Spring 5-12-2018

NANOCOMPOSITES OF POLYPYRROLE AND COBALT OXIDE AS EFFICIENT AND STABLE MULTIFUNCTIONAL MATERIALS FOR SUPERCAPACITORS AND OVERALL WATER SPLITTING

AHLAM ALGHAMDI
ahlam.alghamdi@gus.pittstate.edu

NANOCOMPOSITES OF POLYPYRROLE AND COBALT OXIDE AS EFFICIENT AND STABLE MULTIFUNCTIONAL MATERIALS FOR SUPERCAPACITORS AND OVERALL WATER SPLITTING

A Thesis Submitted to the Graduate School
in Partial Fulfillment of the Requirements
for the Degree of
Master of Science

Ahlam Alghamdi

Pittsburg State University

Pittsburg, Kansas

May, 2018

NANOCOMPOSITES OF POLYPYRROLE AND COBALT OXIDE AS EFFICIENT AND STABLE MULTIFUNCTIONAL MATERIALS FOR SUPERCAPACITORS AND OVERALL WATER SPLITTING

Ahlam Alghamdi

APPROVED:

Thesis Advisor _____
Dr. Ram Gupta, Department of Chemistry

Committee Member _____
Dr. Khamis Siam, Department of Chemistry

Committee Member _____
Dr. Pawan Kahol, Department of Physics

Committee Member _____
Dr. John Franklin, Department of English and Modern Languages

ACKNOWLEDGEMENTS

First and foremost, I would like to thank God Almighty for giving me the opportonity, strength, cognition and capability to undertake this research study and to persevere and complete it successfully. Also, I would like to take this opportunity to express my thanks and gratitude to some persons who contributed to encourage me to achieve this research.

I would first like to thank my thesis advisor Prof. Ram Gupta, the graduate coordinator of Polymer Chemistry at Pittsburg State University. The door of Professor Gupta's office was always open whenever I had a concerns about my research work or questions about my thesis writing. His guidance, advice, immense knowledge and motivation were always available for me.

Moreover, I would like to thank my committee members, Professor Khamis Siam, Professr Pawan Kahol and Professor John Franklin and all other faculty members in the Chemistry Department at Pittsburg State University. Additionally, I would like to thank Dr. Sanjay Mishra, for recording SEM images at the University of Memphis.

Finally, I would like to extend my special thanks and gratitude to my husband Abdulrahman and my family for their patience, reassurance and unlimited support. I would like to dedicate this work to my baby girl Deema, I hope to be a source of pride for her.

NANOCOMPOSITES OF POLYPYRROLE AND COBALT OXIDE AS EFFICIENT AND STABLE MULTIFUNCTIONAL MATERIALS FOR SUPERCAPACITORS AND OVERALL WATER SPLITTING

An Abstract of the Thesis by
Ahlam Alghamdi

The main objective of this study is to synthesize nanostructured cobalt oxide decorated on polypyrrole using a facile method for energy applications. For this, polypyrrole was first synthesized using a chemical polymerization method. In the second step, a varying amount of cobalt oxide was decorated on polypyrrole using a hydrothermal process. The synthesized materials were structurally and electrochemically characterized. It was observed that the electrochemical properties of the composites depend on their composition. The optimized composition showed a maximum specific capacitance of 1533 F/g at 1 mV/s with a significant electrochemical stability. The composite retained ~87% of its initial charge storage capacity even after 5,000 cycles of charging-discharging studies. Moreover, these composites showed outstanding performance as an electrocatalyst for oxygen and hydrogen evolution reactions. It required an overpotential of 316 mV and 132 mV to achieve a current density of 10 mA/cm^2 for oxygen and hydrogen evolution reactions, respectively. Furthermore, cobalt sulfide was synthesized using the pervious composite (not carbonized) to compare the water splitting activities for both cobalt oxide and cobalt sulfide. Clear improvement was obtained for cobalt sulfide based on oxygen evolution reaction and hydrogen evolution reaction. Our results suggest that composites of cobalt oxide and polypyrrole can be used as bi-functional materials for energy applications such as for supercapacitors and electrocatalysts for water splitting.

TABLE OF CONTENTS

CHAPTER PAGE

List of Tables

List of Figures

CHAPTER I

INTRODUCTION

1.1. Importance of renewable and green energy:

Population growth has created the demand for eco-friendly multi-functional energy generation and storage systems. The interest for fuel assets and issues concerning global warming has made energy stockpiling and generation from sustainable resources of greater importance. Finding a source of energy is no longer the only goal. The traditional source of energy is usually based on oil or carbon, which negatively affects the environment. Global warming and pollution are notable indicators of environmental damages. Nowadays, scientists are interested in finding green, renewable energy sources that are more secure, accessible and inexpensive. According to Ibrahim et al.[1], in the next 10 to 20 years all energy systems should be based on renewable resources. Solar energy and wind energy are the most important examples of renewable energies.[2] The limitation of using these types of energies during sunshine or windy weather is considereda drawback.[3] However, energy storage applications which can store these renewable energies could be a great solution because it allows using them at any time and under any conditions. Furthermore, the applications of green energy generation is the other solution to reducing traditional resources usage.

1.2. Energy storage applications:

With the increase of green energy exploitation and their dependence on weather conditions, it is necessary to find more efficient applications to store that energy. As known, there are different energy storage devices such as fuel cells, batteries and electrochemical supercapacitors.

Supercapacitors have become very popular in recent years as an outstanding device among the energy storage applications because of their characteristic features and simplistic model.

1.2.1. Supercapacitor:

A supercapacitor has similarities with capacitors and batteries, without any chemical reaction. The electric field is a responsible factor for operating the supercapacitor.[1] Supercapacitors are able to generate energy density higher than conventional capacitors and power density greater than fuel cells and batteries as seen in Figure 1.1.[4] Moreover, supercapacitors have several advantages which make them more attractive, such as long cycle life, fast charging-discharging, high power density and high specific capacitance.[5–10] In terms of the charge-storage mechanism, supercapacitors are classified into two types: electrochemical double layer capacitors (EDLCs) and pseudocapacitors. The supercapacitors which use both types of energy storage mechanisms are referred to as hybrid capacitors. The charge storage capacity in EDLCs depends on the diffusion and accumulation of the electrostatic charge at the interface of electrode/electrolyte. Carbon-based materials are used in this type of supercapacitor.[11,12] On the other hand, pseudocapacitors depend on Faradic reactions which are reversible and provide energy storage capacity quickly and much greater than EDLC.[11] Metal oxides, hydroxides and conducting polymers are usually used in pseudocapacitors because of their pseudocapacitive properties.[13,14]

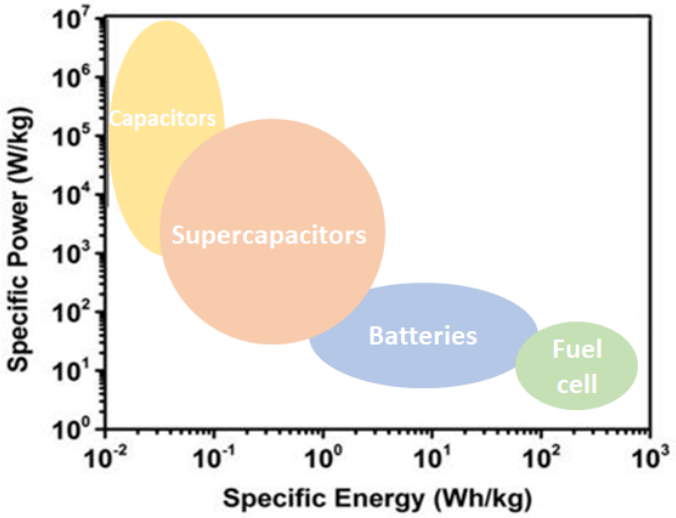

Figure 1.1. Ragone plot for energy density versus power density.

1.3. Green energy generation:

The disadvantages and limitations of the traditional energy generating methods led to finding more efficient green methods which are inexpensive and environmentally friendly. Energy generation through water splitting is a new approach to efficiently utilize green energy. Recently, water splitting became an attractive way to generate hydrogen as a fuel and oxygen as a breathable gas.[15] There is abundant research which proves how it is considered a successful method.[16–25] Advanced materials for water splitting electrolysis are centralized in a renewable energy system, including oxygen evolution reaction (OER) and hydrogen evolution reaction (HER)[26]. Figure 1.2 shows the schematic of water splitting to generate green energy. Thermodynamically, water splitting should occur at 1.23 V (vs. RHE). There is a need for high-quality materials for electrolysis, to ensure minimum energy loss because of the required overpotentials by the half-cell reactions, with OER at the anode and HER at the cathode. Noble-metal based materials such as iridium/ruthenium oxides for OER and Pt for HER are the most efficient electrocatalysts for water splitting [27]. However, they are rare and costly, which limits their potential applications. Recently, metal oxides, hydroxides, sulfides and phosphides have shown higher electrocatalytic activities for

OER and HER. Furthermore, they are abundant, and are inexpensive while still providing superior electrical conductivity.

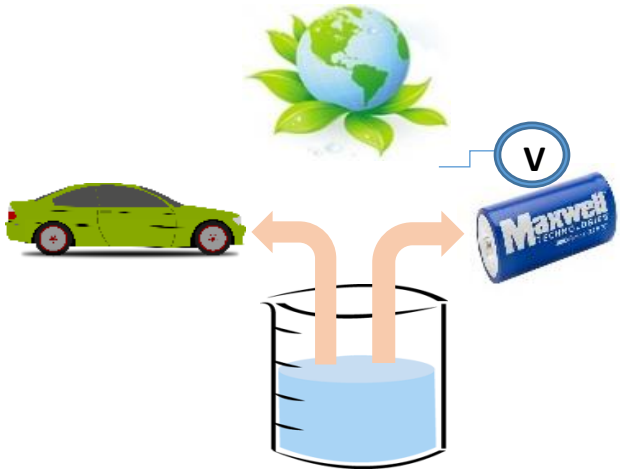

Figure 1.2. Schematic of water splitting to generate green energy.

1.4. Polypyrrole and cobalt oxide:

In terms of multi-functional materials, conducting polymers and metal oxides are suitable materials to be used for energy storage/generation applications. Conducting polymers (CPs) such as polyaniline and polypyrrole have been successfully used as active materials for supercapacitor applications. Among CPs, polypyrrole is the most promising polymer for electrochemical storage application due to its high energy storage capacity, electrochemical stability, environmental friendliness, low cost, easy preparation, high electrical conductivity and fast charge-discharge kinetics.[28–30] On the other hand, transition metal oxides are considered as the best materials for pseudocapacitors. Among transition metal oxides, cobalt oxide is very promising due to its high theoretical specific capacitance and good electrochemical conductivity.[31,32] Even though metal oxides have high capacitance, they are not very electrochemically stable due to the Faradic reaction involved in the charge storage mechanism. A possible solution is to use composites of conducting polymers and metal oxides to achieve high performance materials for energy applications.[9,33–35]

1.5. Objective of this research:

The main objective of this research is to obtain high efficiency and bi-functional material which could be used for energy storage as well as energy generation application. Nanocomposites of polypyrrole and cobalt oxide were prepared using chemical polymerization and hydrothermal method. The effect of composition on the charge storage and water splitting was studied in detail.

CHAPTER II

EXPERIMENTAL DETAILS

2.1. Materials:

Pyrrole (Py) was purchased from Sigma-Aldrich, USA and used without further purification. Other reagents such as hexadecyl trimethyl ammonium bromide (CTAB), hydrochloric acid (HCl), ammonium persulphate ($(NH_4)_2S_2O_8$), urea were also purchased from Sigma-Aldrich, USA. Cobalt nitrate ($Co(NO3)_2$) was purchased from Strem Chemicals, USA. Sodium Sulfide ($Na_2S.\ 9H_2O$) was purchased from Acros Organic, USA. The other chemicals for the prepration of electrodes such as polyvinylidene fluoride (PDVF), 1-Methyl-2 pyrrolidone, acetylate black and Ni foam were purchased from MTI corporation, USA.

2.2. Synthesis of polypyrrole (Ppy):

Polypyrrole was synthesized using the chemical polymerization method. In typical synthesis, 4.548 g of CTAB and 63 mL of HCl (12 mol/l) were added to 312 ml of DI water and stirred for 0.5 h. Then 3 ml pyrrole was added to the mixture with vigorous stirring. The solution was stirred for an additional 2 h. Then 60 ml of $(NH_4)_2S_2O_8$ (0.83 M) solution was added dropwise to the above solution to polymerize the pyrrole. The reaction was continued at room temperature for an additional 1 h. Finally, the black precipitate was filtered and washed with DI water. The washed, powdered sample was dried under vacuum at 60 ^oC for 12 h.

2.3. Synthesis of nanocomposites of polypyrrole and cobalt oxide:

The nanocomposites of polypyrrole and cobalt oxide were synthesized using a facile hydrothermal method. In typical synthesis, first some amount of polypyrrole was dispersed in 30

ml of DI water using a bathsonicator for 30 min. After that, 1088 mg of cobalt nitrate was added to the dispersed solution of polypyrrole and sonicated for an additional 30 min. 450 mg of urea was added to the above solution under sonication and sonicated for an additional 30 min. Finally, the entire solution was transferred into a 45 mL Teflon-lined stainless steel autoclave and heated to 180 ^{o}C for 10 h. After cooling to room temperature, the obtained powder was filtered, washed with DI water and dried in a vacuum oven for one day at 60 ^{o}C. Finally, the powder was carbonized at 400 ^{o}C for 2 h at a ramp rate of 5 ^{o}C/min under nitrogen atmosphere. Cobalt oxide was also synthesized using the same procedure without having polyprrole. All the samples were synthesized using the same procedure but with different amounts of polypyrrole as given in Table-1.

Table 1. Details of the chemicals used for the synthesis.

Sample code	Ppy	DI water	$Co(NO_3)_2$	Urea
S1	400 mg	30 mL	-	-
S2	1200 mg	30 mL	1088 mg	450 mg
S3	600 mg	30 mL	1088 mg	450 mg
S4	300 mg	30 mL	1088 mg	450 mg
S5	200 mg	30 mL	1088 mg	450 mg
S6	-	30 mL	1088 mg	450 mg

2.4. Synthesis of cobalt sulfide (sample code-Sulfurized S5):

Nanocomposites of polypyrrole and cobalt oxide were sulfurized to prepare a nanocomposite of polypyrrole and cobalt sulfide. For this, 200 mg of uncarbonized S5 sample was dispersed in 30 ml of DI water and then 320 mg of ($Na_2S.\ 9H_2O$) was added and dissolved. The entire solution was then transferred into a 45 ml Teflon-lined stainless steel autoclave and heated

to 140 ^{o}C for 24 h. After cooling to room temperature, the powder was filtered, washed with DI water and dried in a vacuum oven for 24 h at 60 ^{o}C.

2.5. Structure characterizations:

The synthesized samples were characterized by using various techniques such as X-ray diffraction (XRD), X-ray photoelectron spectroscopy (XPS) and scanning electron microscopy (SEM). The Brunauer-Emmett-Teller (BET) adsorption method was used to determine the surface area of the samples. More details of these techniques are following.

2.5.1. X-Ray Diffraction:

X-ray diffraction technique was used to observe the crystallinity and phase purity of the synthesized samples using a Shimadzu X-ray diffractometer set on the 2θ-θ scan with CuKα λ=1.5406 Å radiation. The X-ray was operated at 40 kV of voltage and a current of 30 mA. 0.2 mm of the slits was used for the sides of source and detector. The X-ray beams were shined directly onto the sample and the diffracted beams were collected and measured while the sample was rotated through the angle range of 2θ = 10°−80°. The X-ray detector was positioned so that the angle between the atomic planes and the detector was 2θ to satisfy the geometry as shown in Figure 2.1.

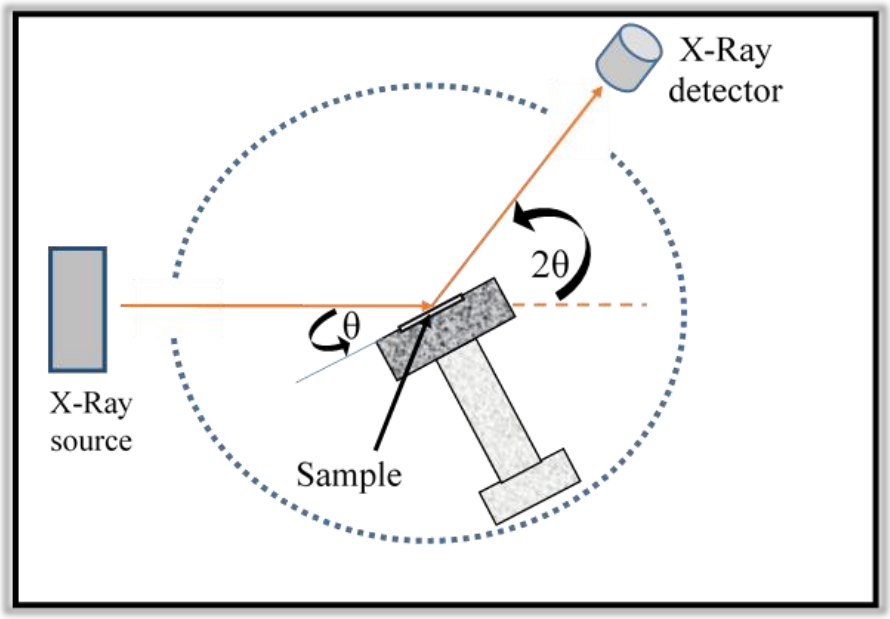

Figure 2.1. Schematic diagram of X-Ray diffraction.

2.5.2. Scanning Electron Microscopy:

The morphology and structure of the synthesized samples were studied using a field-emission scanning electron microscopy. The reason for using this microscope is its ability to read the observations characteristic in nanometers (nm) and micrometers (μm) range. The particle' size and shape for each sample was determined and recorded with help from Dr.Sanjay Mishra at the University of Memphis.

2.5.3. X-ray photoelectron spectroscopy:

Elemental composition of the synthesized materials was determined using X-ray photoelectron spectroscopy. A Thermo Scientific Kα XPS system was used to record XPS spectra. The x-ray power of 75 W at 12 kV was used for the experiment with a spot size of 400 mm^2. The XPS data acquisition was performed using the "Advantage v5.932" software provided with the instrument.

2.5.4. Brunauer–Emmett–Teller Surface Area measurement:

The surface area of the synthesized samples was measured using the BET surface area measurement method. Nitrogen adsorption/desorption isotherms were analyzed after degassing the samples for 24 h at 60 °C using a Micrometrics, USA, ASAP 2020 volumetric adsorption analyzer at 77 K. The BET absorption method was used to determine specific surface area. The photograph of the BET instrument used for this study is given in Figure 2.2.

Figure 2.2. Photograph of the BET instrument.

2.6. Electrochemical measurements:

The electrochemical tests were performed using a standard three-electrode cell system containing a counter electrode, a reference electrode, and a working electrode. Platinum wire and saturated calomel electrodes were used as a counter and reference electrode, respectively. Nickel foams were coated by samples to be used as working electrods. Electrochemical testing for supercapacitors was done in 3M KOH electrolyte, while water electrolysis was performed in 1M KOH electrolyte. The schematic diagram of the three-electrode system is shown in Figure 2.3.

The working electrode was prepared by mixing 80 wt.% of the synthesized sample, 10 wt.% of acetylene black, and 10 wt.% of polyvinylidene difluoride in the presence of N-methyl pyrrolidinone. After mixing the components, the slurry was pasted onto nickel foam and dried at 60 °C under vacuum for 10 h. The loading mass was accurately measured by weighing the nickel foam before and after electrode preparation using an analytical balance (model MS105DU, Mettler Toledo, max. 120 g, 0.01 mg of resolution). Before coating the slurry onto nickel foam, the foam was cleaned using 3M HCl acid, followed by washing with water and acetone. The cleaned nickel foam was dried in the vacuum oven for 1 h at 60 °C. The digital photographs of the prepared electrodes are shown in Figure 2.4. A symmetric supercapacitor device was fabricated by sandwiching an ion transporting layer (Celgard, 25μm thick, 39% porosity) between two S4 electrodes as shown in Figure 2.5. The electrochemical measurements of the device were performed at various temperatures in 3M KOH electrolyte.

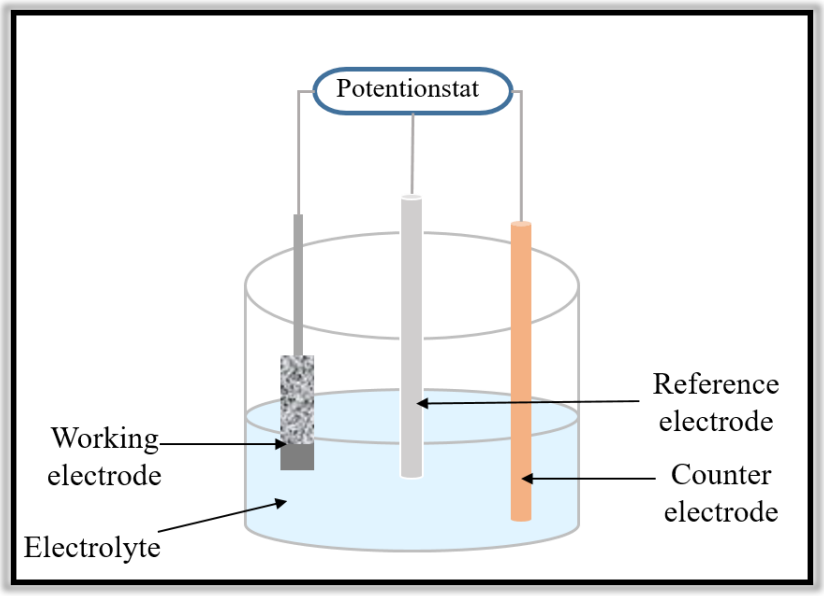

Figure 2.3. Schematic of three electrode system.

Figure 2.4. Picture of working electrodes in a vacuum oven.

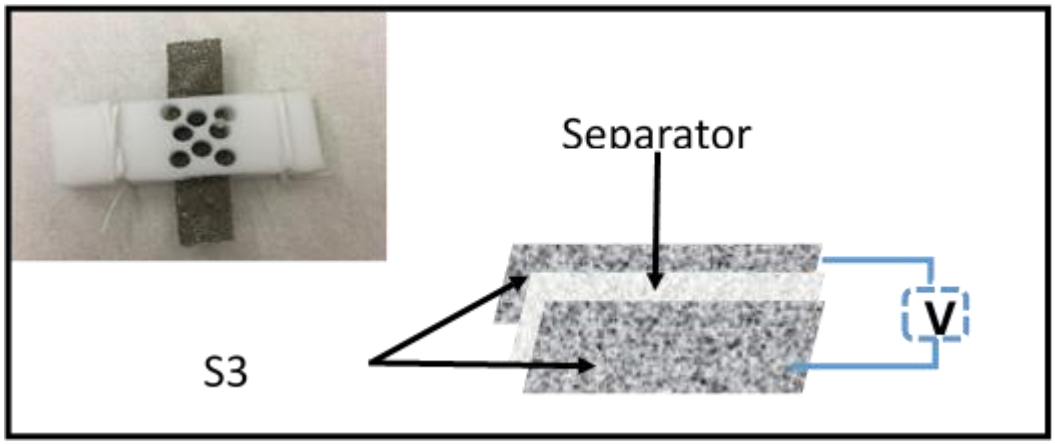

Figure 2.5. Schematic diagram of supercapacitor device with the real picture.

All the electrochemical testing was performed on a Versastat 4-500 electrochemical workstation (Princeton Applied Research, USA). VersaStudio software provided by Princeton Applied Research was used to analyze the electrochemical data. The electrochemical performance of synthesized samples was studied using cyclic voltammetry (CV), galvanostatic charge-discharge (GCD) measurements, and electrochemical impedance spectroscopy (EIS) methods.

2.3.1. Cyclic Voltammetry:

The supercapacitor performance of the synthesized samples was evaluated by a cyclic voltammetry test. CV measurements were carried out at various scan rates (1-300 mV/s) in 0-0.6 V potential range. The supercapacitor device was also tested at various scan rates at room temperature. The effect of temperature on charge storage capacity of the device was studied at a scan rate of 100 mV/s in the temperature range of 10-60 ^{o}C.

2.3.2. Galvanostatic Charge-Discharge Measurements:

The charge storage capacity of the synthesized samples was studied by using galvanostatic charge-discharge measurements. The charge-discharge cycles were carried out in 0-0.6 V potential range at various applied currents (0.5-20 A/g). In the same manner, the supercapacitor device was tested in applied currents 0.3, 0.4, 0.5, 0.75 and 1 A/g at room temperature and in applied current equal to 0.75 A/g at a temperature range of 10-60 ^{o}C.

2.3.3. Electrochemical Impedance Spectroscopy:

The synthesized samples' impedance analysis was determined by using an impedance analyzer with an amplitude of 10 mV in 0.05- 10,000 Hz frequency range. Moreover, the effect of temperature on the electrochemical behaviors of the supercapacitor device was also studied. The purpose of these synthesized samples as an electrocatalyst for oxygen evolution reaction and hydrogen evolution reaction was also examined. To illustrate, the water electrolysis could provide hydrogen which could be used as fuel, and oxygen which could be released into the atmosphere as a breathable gas as shown in Figure 2.6. Thermodynamically, water splitting should occur at 1.23 V, but practically it occurs at a higher potential called overpotential. The water splitting is described by the following electrochemical reaction[36]:

$$2H_2O \rightarrow 2H_2 + O_2$$

The OER activity of the sample electrode was conducted using linear sweep voltammetry (LSV) in 1 M KOH electrolyte at a scan rate of 2 mV/s in 0.14 – 0.84 V potential range, while the HER activity was carried out at a scan rate of 2 mV/s in -0.9 – -1.5 V potential range. The

electrochemical impedance spectra were also studied to understand the charge-transport mechanism.

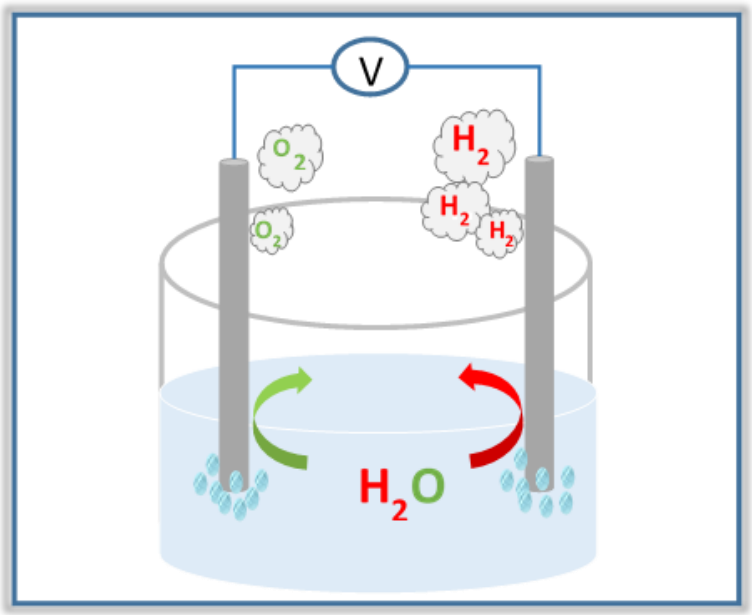

Figure 2.6. Schematic represents water splitting where the gases of oxygen and hydrogen are produced.

CHAPTER III

RESULTS AND DISCUSSION

3.1. Structure characterization:

3.1.1. X-ray diffraction analysis:

The powder X-ray diffraction technique was used to determine the phase purity and crystallinity of the synthesized samples. A broad characteristic peak due to amorphousness of the sample S1 was observed as shown in Figure 3.1. All the cobalt-based nanocomposites showed presence of mixed phases of cobalt oxides as shown in Figure 3.3- 3.6. XRD patterns showed presence of $Co(OH)_2$ and CoO phases which could be due to low temperature annealing of the samples. The majority of the peaks were corresponding to the face-centered cubic structure of Co_3O_4. Figure 3.7 shows the XRD patterns of the sample obtained after sulfurizing S5 sample. All the observed peaks match well with the cubic structure of Co_9S_8.

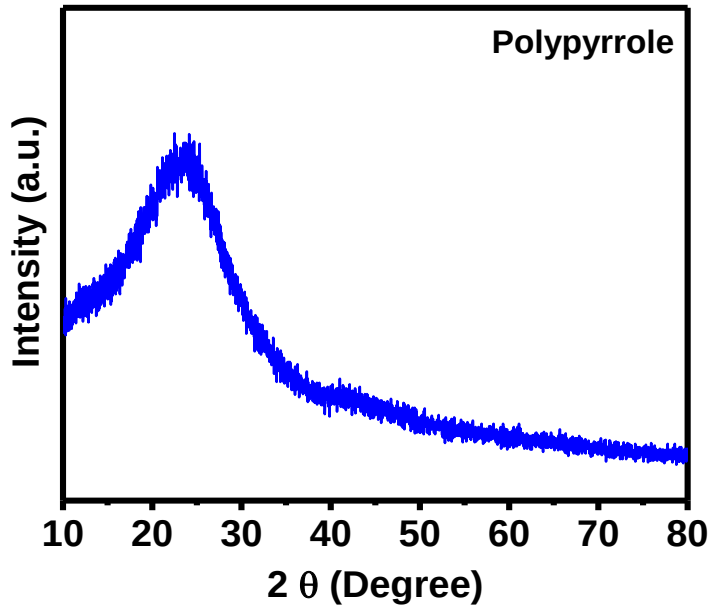

Figure 3.1. XRD patterns of sample S1.

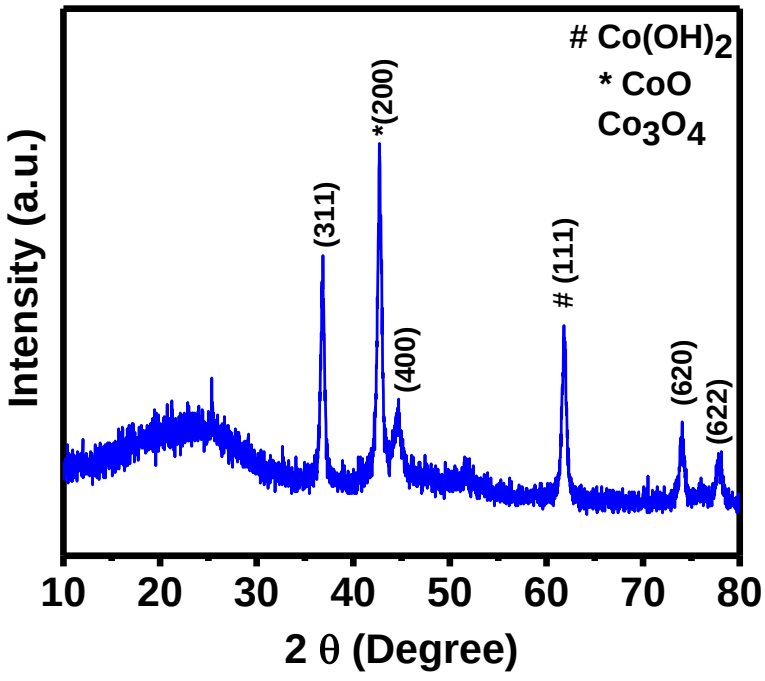

Figure 3.2. XRD patterns of sample S2.

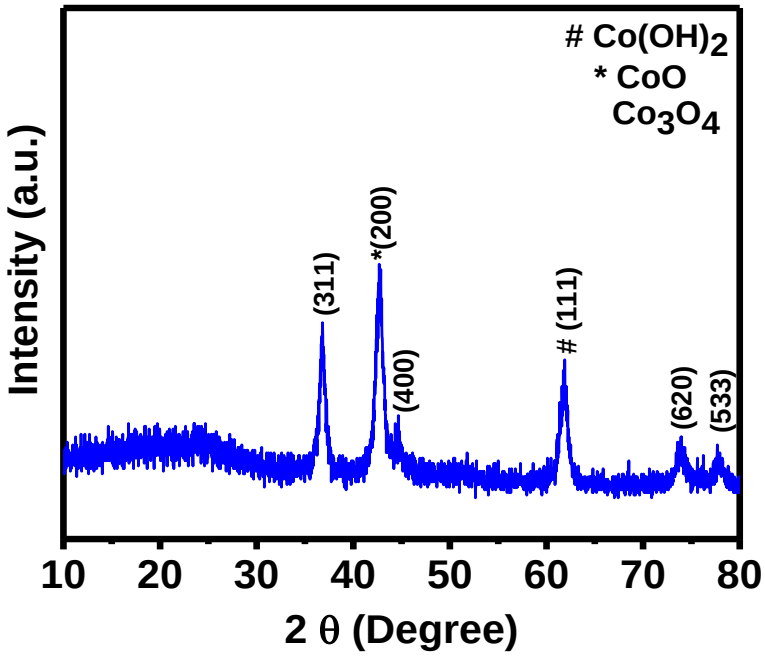

Figure 3.3. XRD patterns of sample S3.

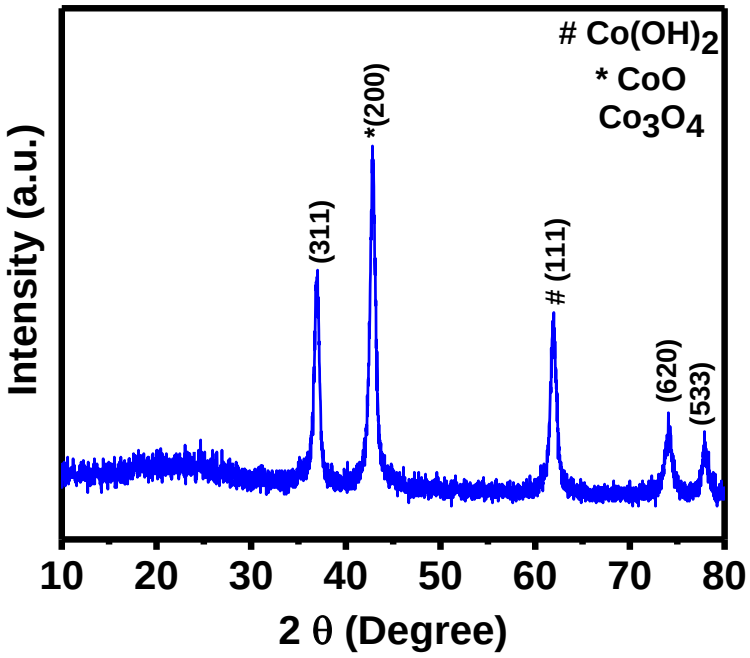

Figure 3.4. XRD patterns of sample S4.

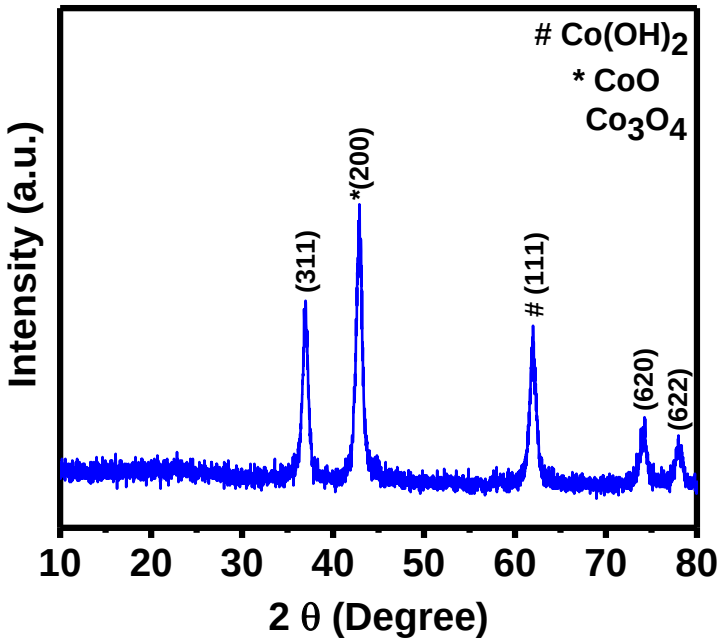

Figure 3.5. XRD patterns of sample S5.

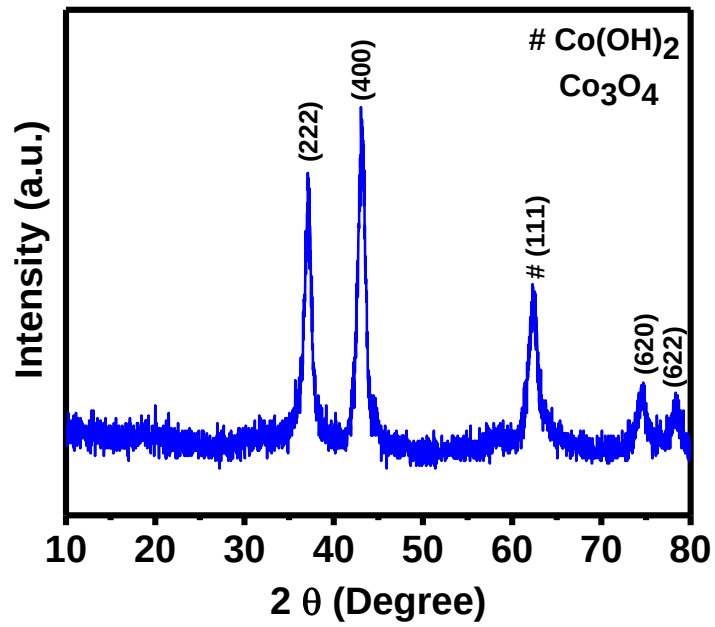

Figure 3.6. XRD patterns of sample S6.

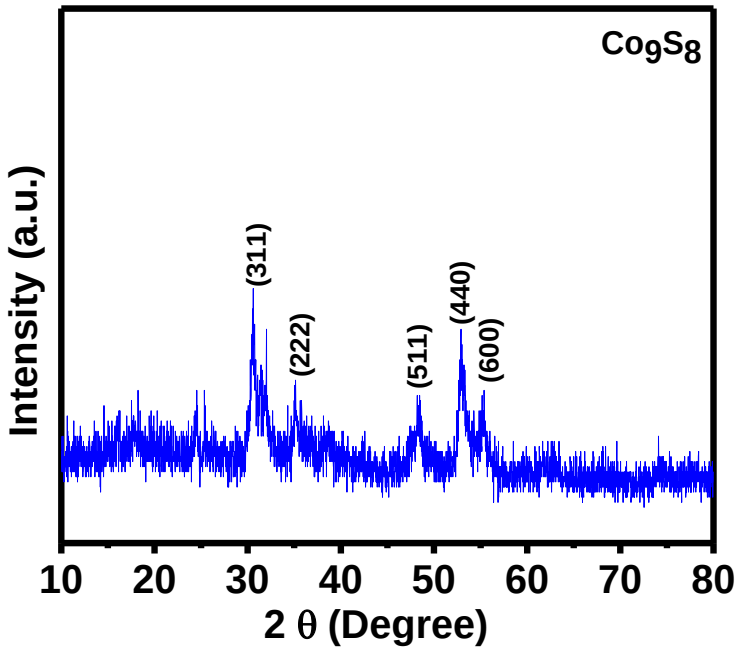

Figure 3.7. XRD patterns of sample sulfurized S5.

3.1.2. Scanning Electron Microscopy:

The morphology and structure of all the synthesized samples were determined using scanning electron microscopy. Figure 3.8 show the SEM images S1 sample at various magnifications. As can be seen, the sample is highly porous in nature, resembling naturally porous stones. The SEM images of the nanocomposites of polypyrrole and cobalt oxides are shown in Figures 3.9- 3.12. It is observed that the morphology of the nanocomposites depends on the concentration of cobalt oxide. For example, the sample with lower concentrations of cobalt oxide produced spherical-like particles with the presence of nanorods on the surface as shown in Figure 3.9 and Figures 3.10. On the other hand, higher concentrations of cobalt oxide looked like multiple layered sheets structured, as seen in Figures 3.11 and Figures 3.12. The cobalt oxide without polypyrrole (sample S6) showed a similar morphology (Figure 3.13) as was observed for the samples with higher concentrations of cobalt oxide. The sulfurized nanocomposites of polypyrrole

and cobalt oxide showed a sheet-like structure (Figure 3.14) which was very similar to the structure of the S5 sample.

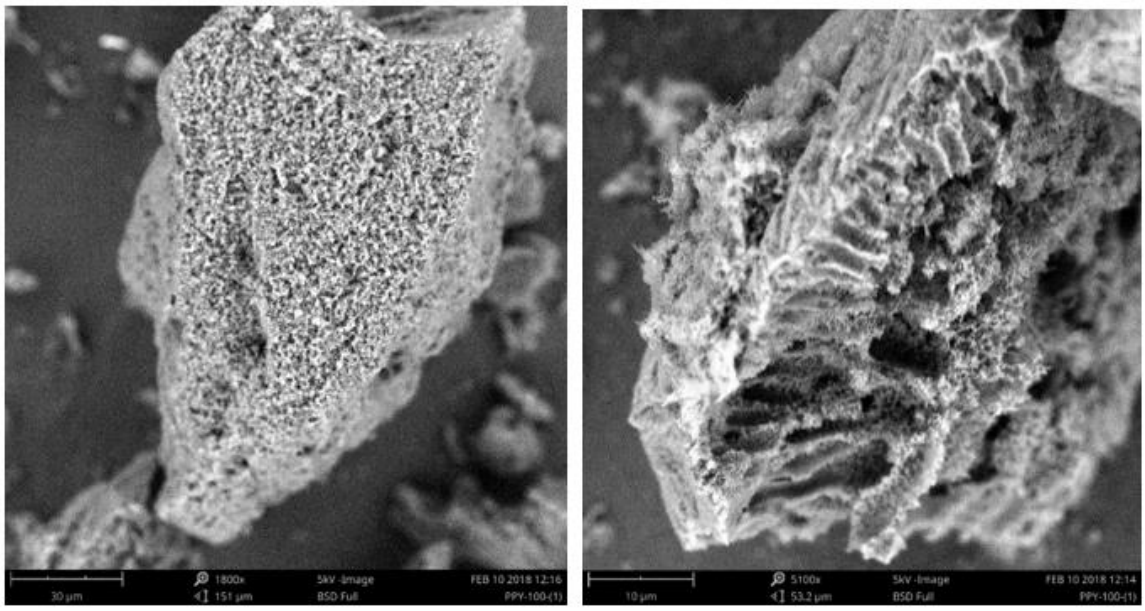

Figure 3.8. SEM images of sample S1 at different magnifications.

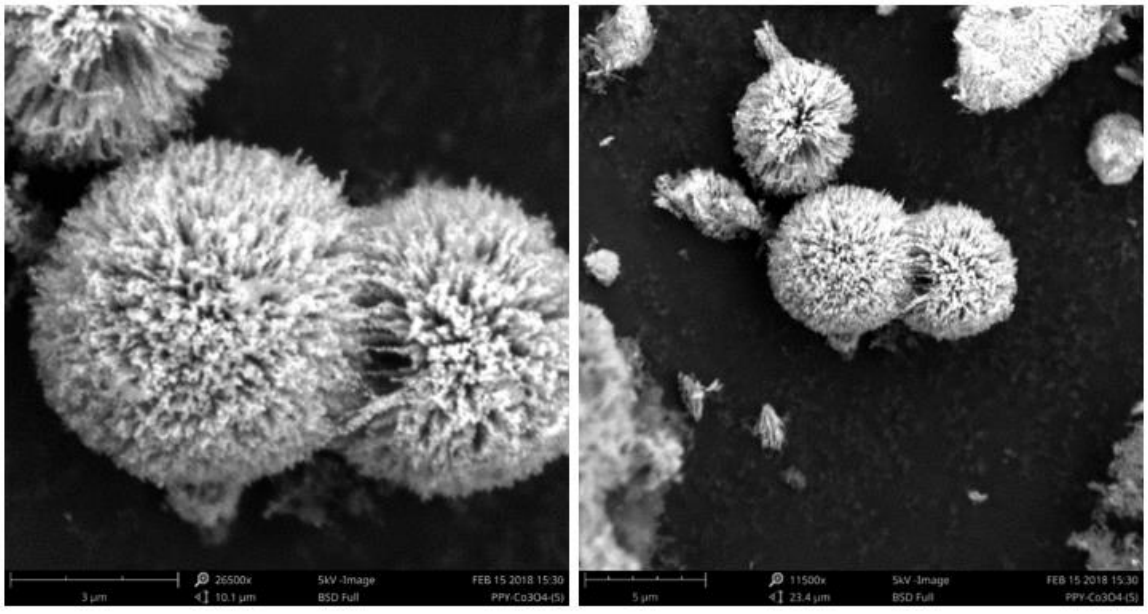

Figure 3.9. SEM images of sample S2 at different magnifications.

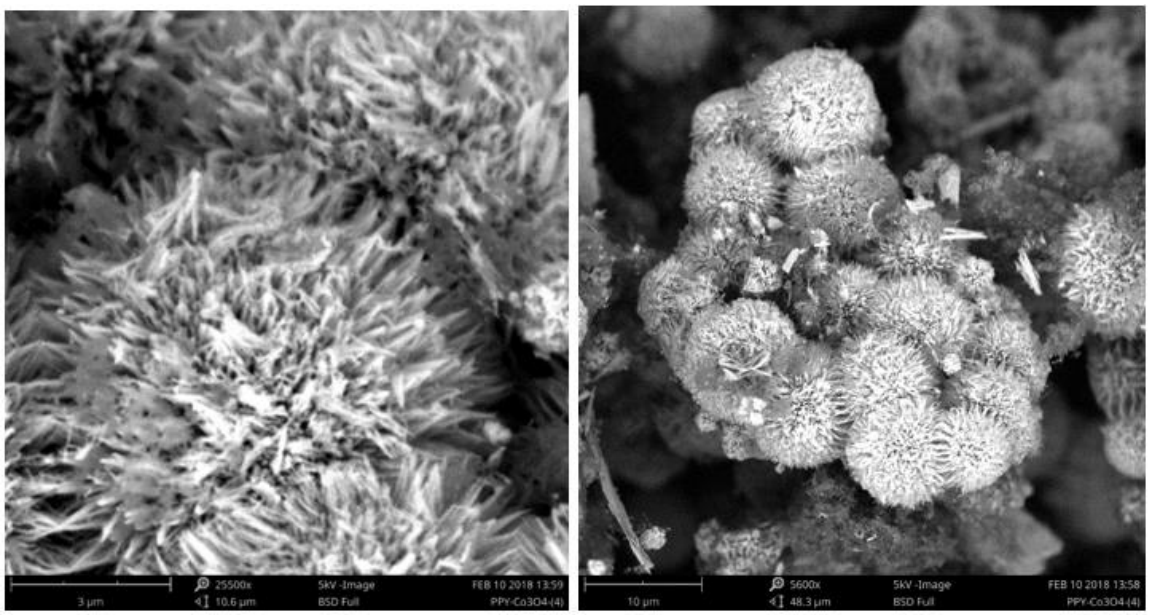

Figure 3.10. SEM images of sample S3 at different magnifications.

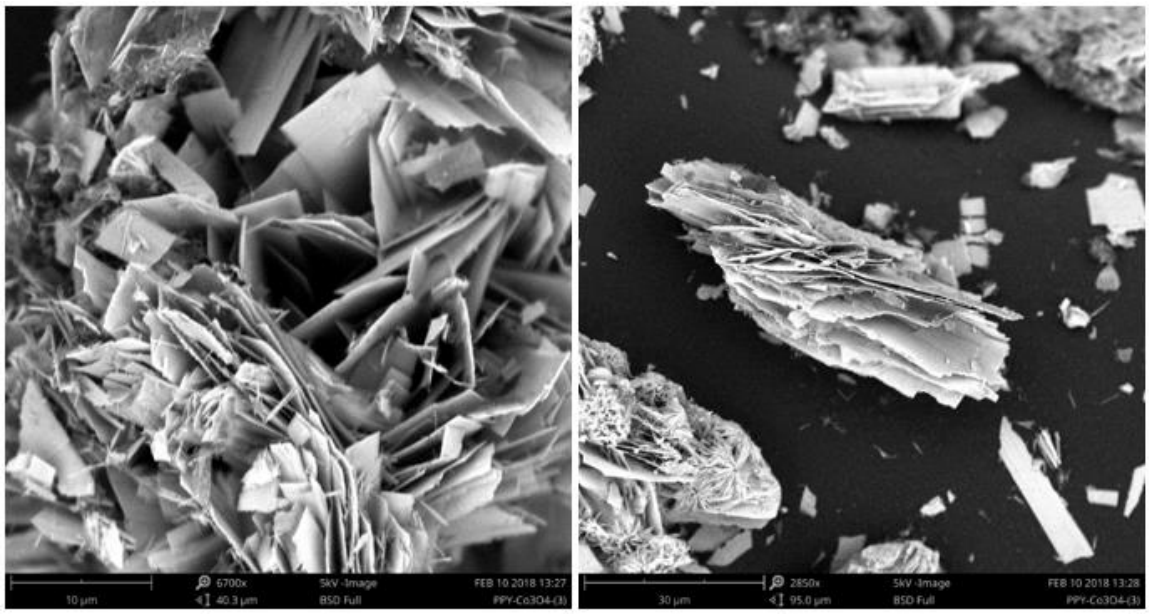

Figure 3.11.SEM images of sample S4 at different magnifications.

Figure 3.12. SEM images of sample S5 at different magnifications.

Figure 3.13. SEM images of sample S6 at different magnifications.

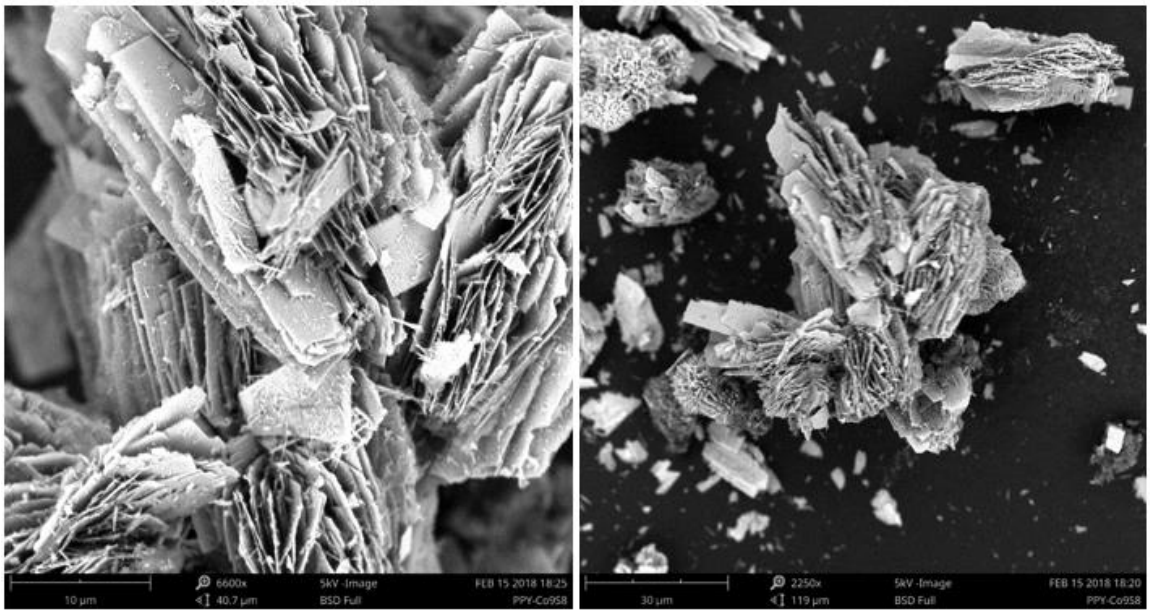

Figure 3.14. SEM images of sample sulfurized S5 at different magnifications.

3.1.3. X-ray photoelectron spectroscopy:

X-ray photoelectron spectroscopy was used to study the chemical nature of the prepared nanocomposites of polypyrrole and cobalt oxide before and after sulfurization. Figure 3.15 and Figure 3.16 show the survey-scan spectrum of S5 and sulfurized S5 samples. The presence of Co, O, N and C in S5 sample and Co, O, N, C and S in sulfurized S5 sample is quite evident.

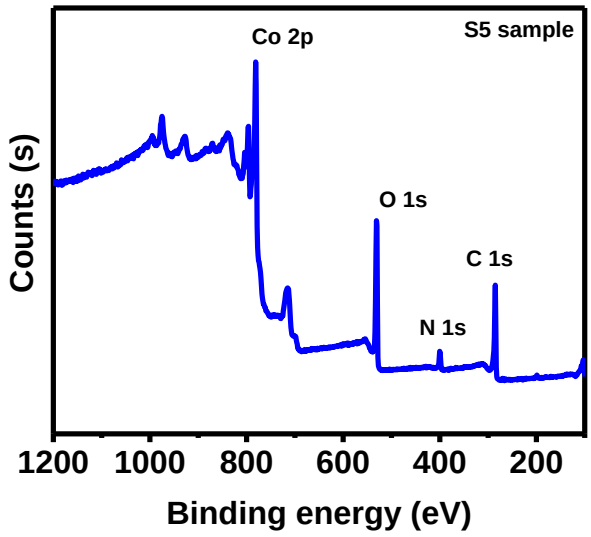

Figure 3.15. XPS survey spectra of S5 sample.

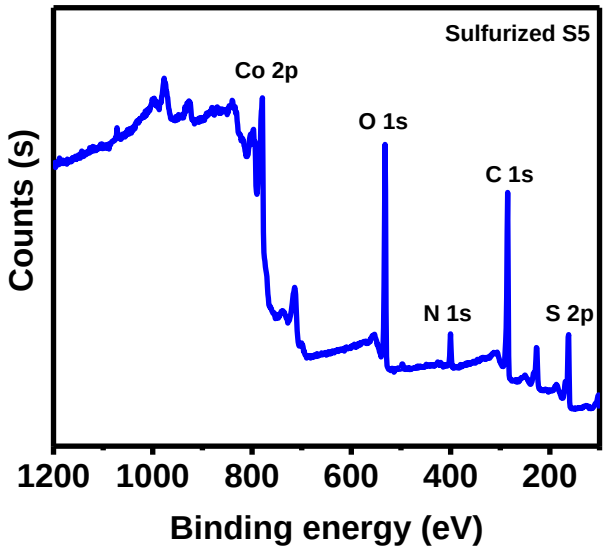

Figure 3.16. XPS survey spectra of sulfurized S5 sample.

In the high resolution spectrum of the Co 2p region for sample S5 and sulfurized S5 (Figure 3.17. and 3.18), the Co 2p3/2 and Co 2p1/2 peaks are deconvoluted into four components corresponding to Co^{+3} and Co^{+2}. The deconvolution of the O 1s spectra (Figure 3.19 and 3.20) confirm the existence of a metal oxygen bond at 529.7 eV in the spinel Co_3O_4.[37] The other observed

peaks are associated with the oxygen of OH^- and the H_2O adsorbed onto the surface. Figure 3.21 and Figure 3.22 represent the C 1s spectra of S5 and sulfurized S5 samples, respectively. The peak at 284.6 eV represents C-C and C-H bonds, while peaks at 285.5 and 288.2 eV could be assigned to carbon-net defects and different oxygen-containing moieties, respectively.[38] The N 1s spectra of sample S5 and sulfurized S5 samples showed two peaks at 400.1 and 398.6 eV which correspond to pyrrolic nitrogen and pyridinic nitrogen respectively (Figure 3.23 and 3.24). In the S 2p spectrum of sample sulfurized S5, a peak at 161.6 eV corresponds to cobalt sulfide. The peaks at 163.7 and 164.9 eV correspond to carbon-bonded sulfur, which demonstrates the successful doping of S into C atoms as shown in Figure 3.25.

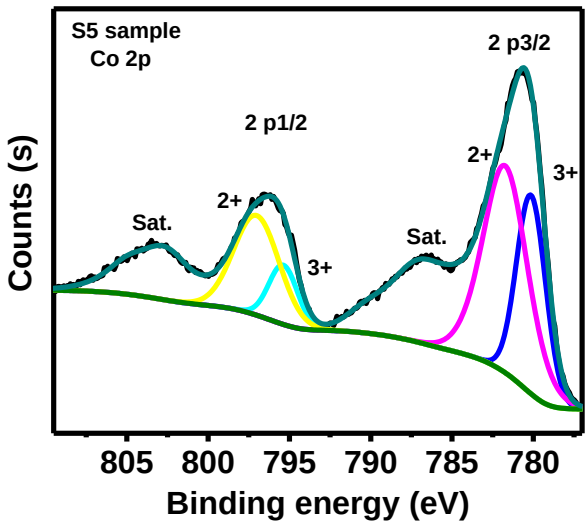

Figure 3.17. XPS spectra of Co 2p for S5 sample.

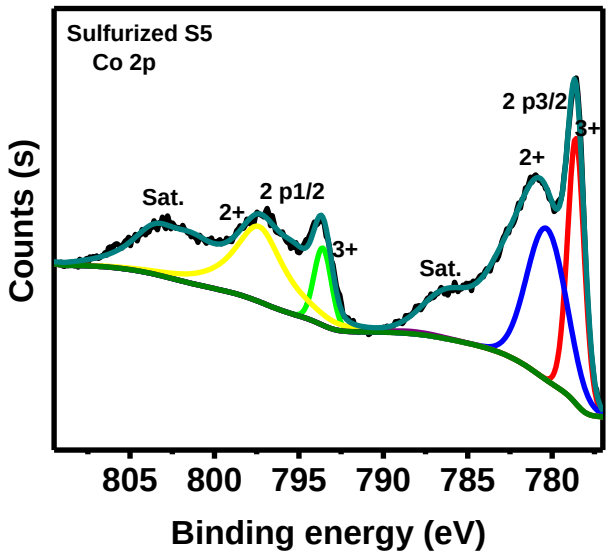

Figure 3.18. XPS spectra of Co 2p for sulfurized S5 sample.

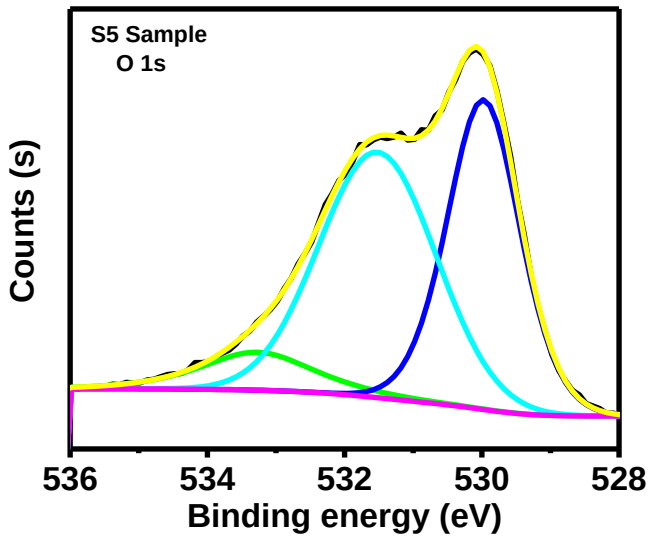

Figure 3.19. XPS spectra of O 1s for S5 sample.

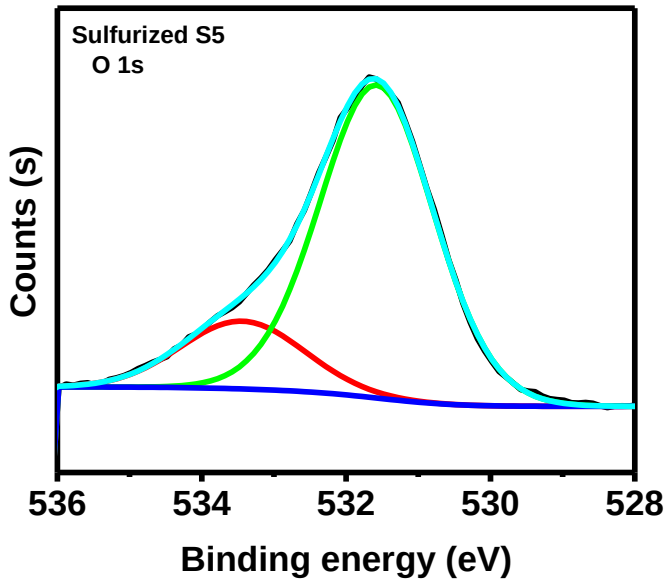

Figure 3.20. XPS spectra of O 1s for sulfurized S5 sample.

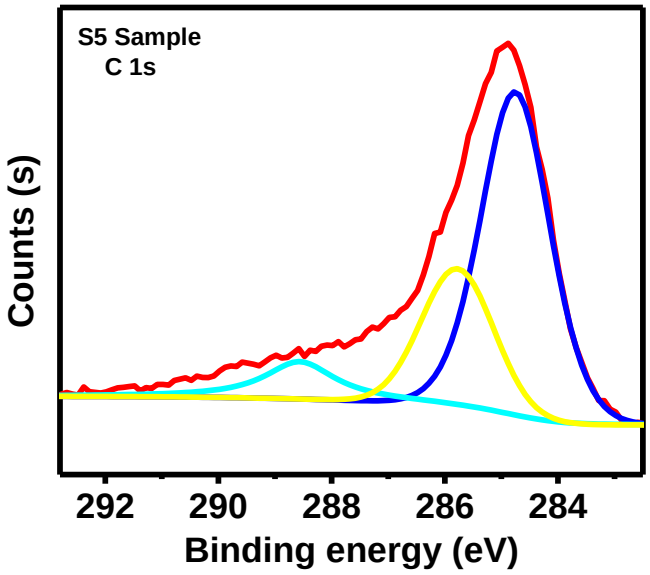

Figure 3.21. XPS spectra of C 1s for S5 sample.

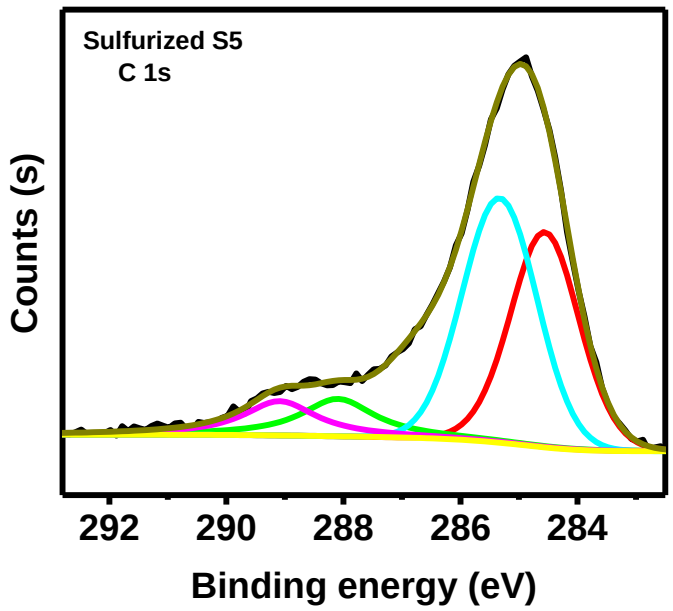

Figure 3.22. XPS spectra of C 1s for sulfurized S5 sample.

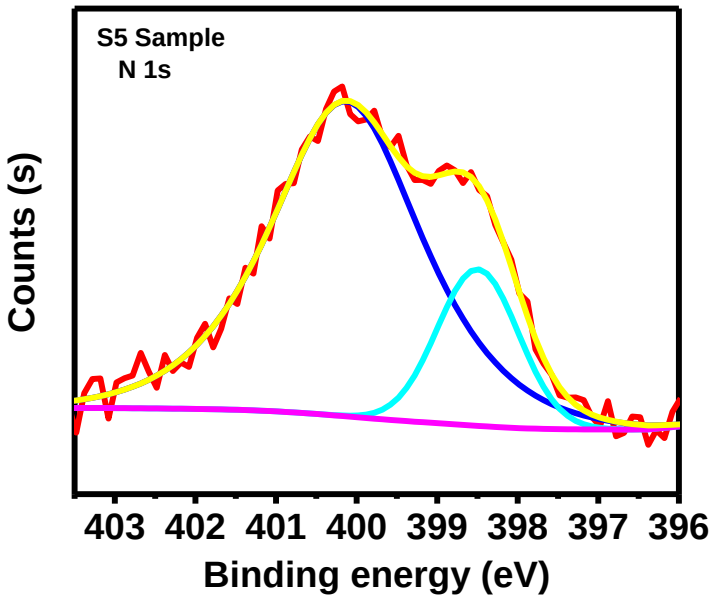

Figure 3.23. XPS spectra of N 1s for S5 sample.

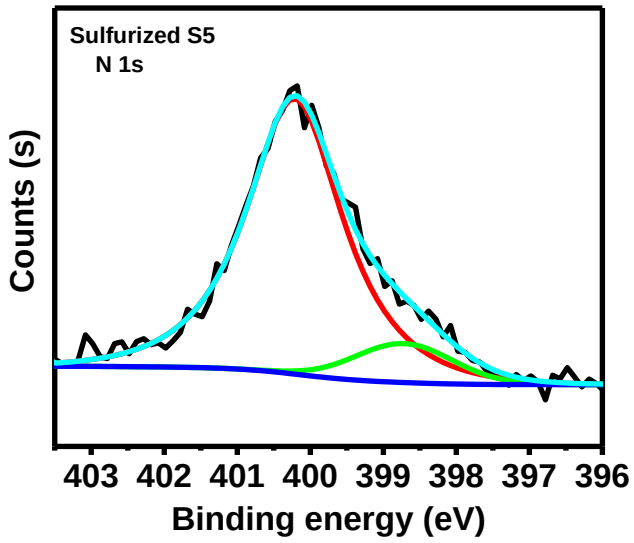

Figure 3.24. XPS spectra of N 1s for sulfurized S5 sample.

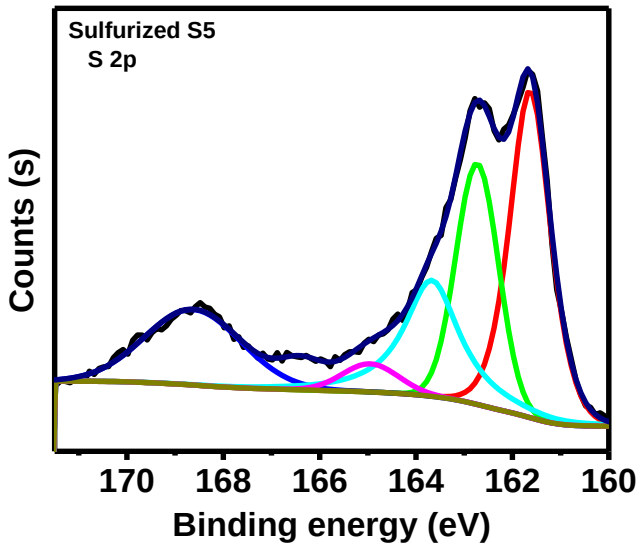

Figure 3.25. XPS spectra of S 2p for sulfurized S5 sample.

3.1.4. Surface area measurements:

The nitrogen adsorption–desorption isotherms and surface area of synthesized samples were studied using Brunauer–Emmett–Teller Surface Area measurement. All studied samples showed a combination of type I and IV isotherm curves as shown in all BET N_2 adsorption–

desorption isotherm figures[39]. S1, S3, S4 and S5 in Figures 3.26- 3.29 display the majority of N_2 adsorption at relative pressures (P/P_o) 0.9 to 1.0 with high slope, while the noticeable hysteresis loops for all of them appear at lower relative pressure (P/P_o). The majority of N_2 adsorption for S6 at relative pressures (P/P_o) 0.6 to 0.8 with distinguishable hysteresis curve, followed by slight incensement in N_2 adsorption, as shown in Figure 3.30. The sulfurized S5 sample shows the majority adsorption at relative pressures (P/P_o) 0.9 to 1.0 with high slope, the hysteresis loop appears at relative pressure (P/P_o) 0.5 to 1.0 as shown in Figure 3.31. All surface areas of all samples are shown in Table 3.1. It is obvious that the specific surface areas of the synthesized materials are influenced by the mass ratio of the polypyrrole. S1 (100% polypyrrole) has shown the highest surface area and S6 (100% Co_3O_4) has shown the lowest 153 m^2/g, 66 m^2/g, respectivly. The optimum combination of plypyrrole and Co_3O_4 represented in S5 the best sample for water splitting activities and S4 the best sample for energy storage, 80 m^2/g and 82 m^2/g respectively. Moreover, their surface areas are lower than S1 and higher than S6. The surface area for S3 is 93 m^2/g since it contains a higher amount of polypyrrole. However, sulfurized S5 sample shows the lowest surface area among all synthesized sample 38 m^2/g, even the improvement obtained in electrocatalysis activity.

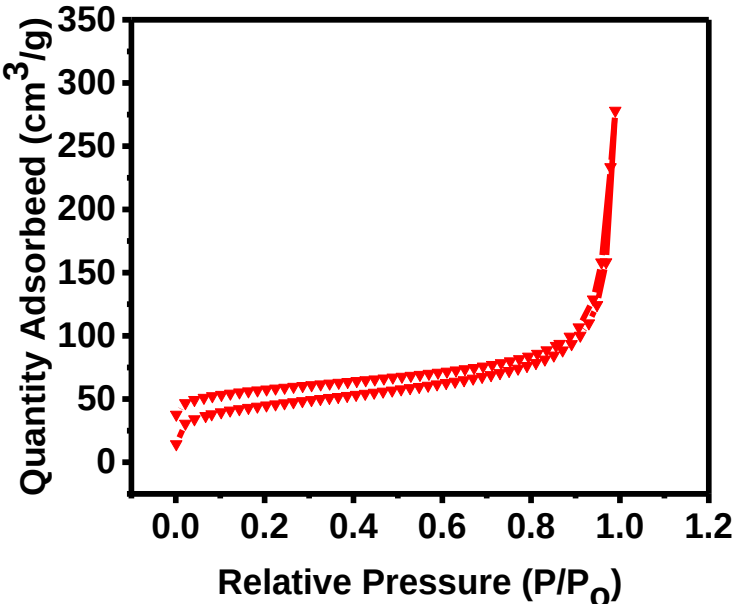

Figure 3.26. Nitrogen adsorption–desorption isotherms of S1.

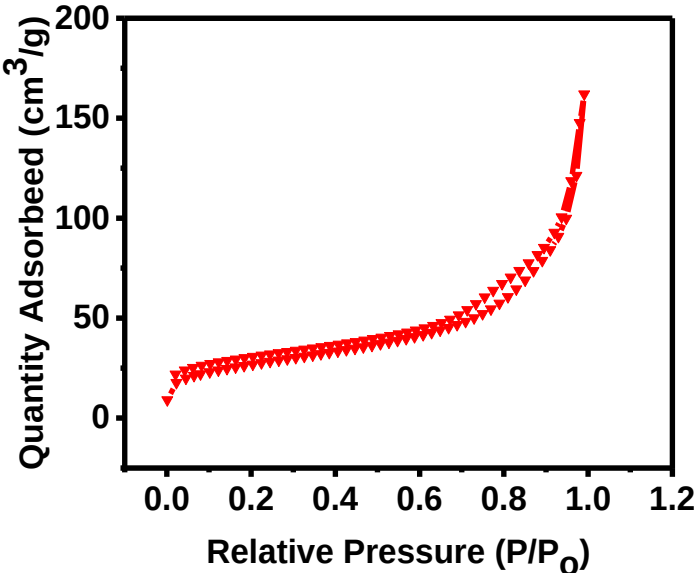

Figure 3.27. Nitrogen adsorption–desorption isotherms of S3.

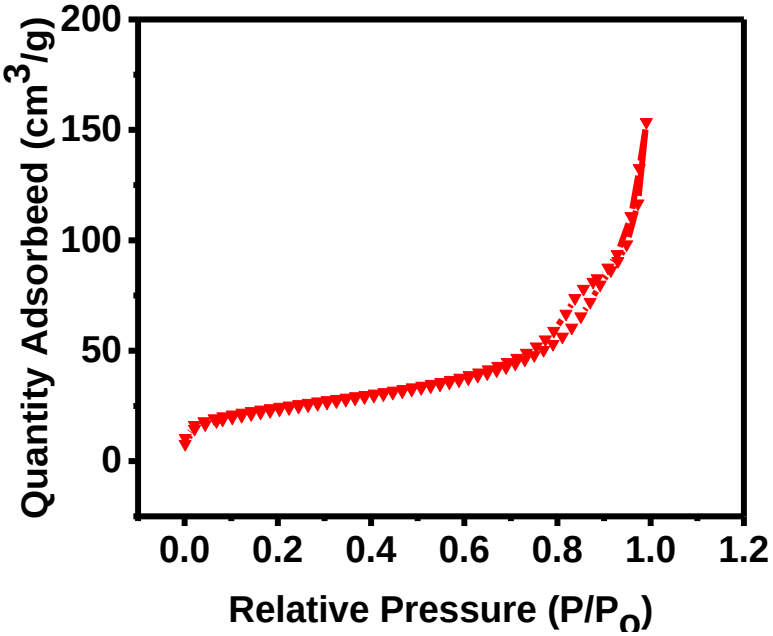

Figure 3.28. Nitrogen adsorption–desorption isotherms of S4.

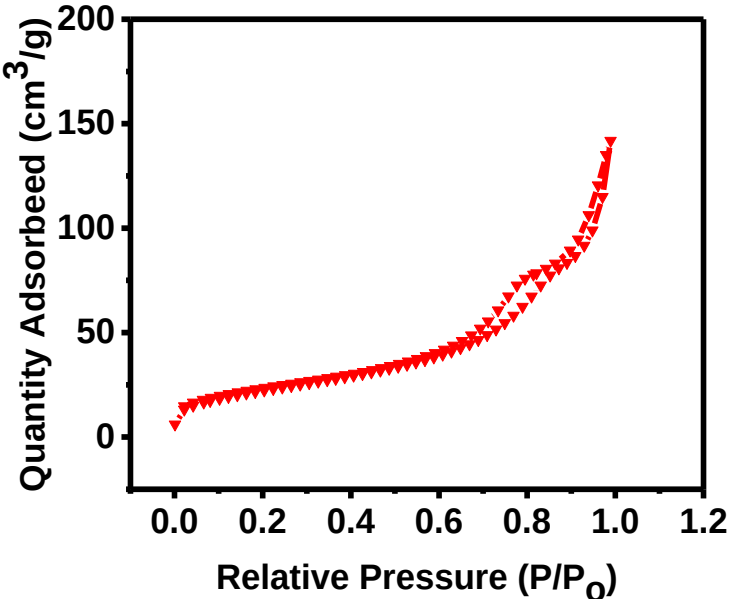

Figure 3.29. Nitrogen adsorption–desorption isotherms of S5.

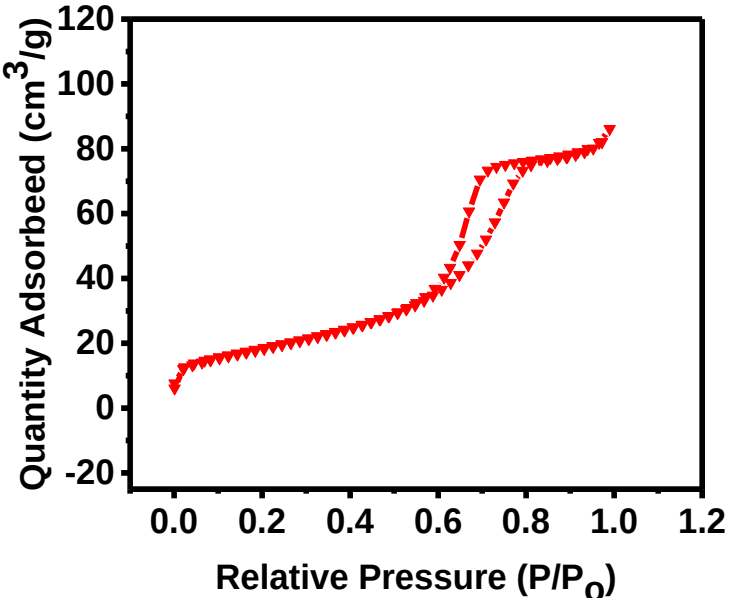

Figure 3.30. Nitrogen adsorption–desorption isotherms of S6.

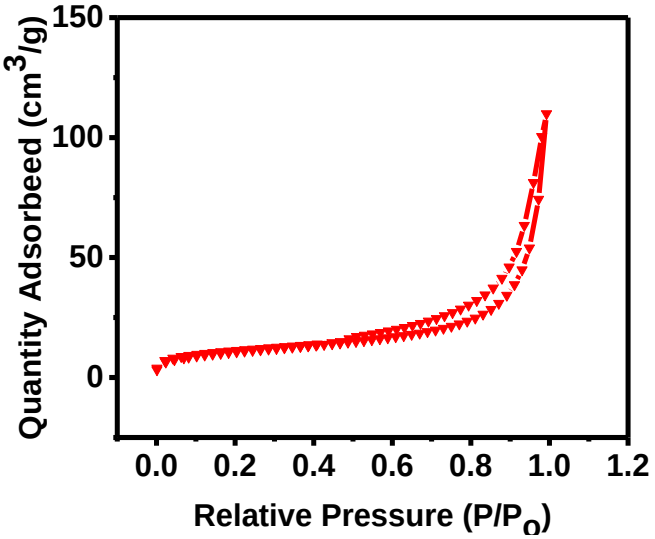

Figure 3.31. Nitrogen adsorption–desorption isotherms of sulfurized S5.

Table 2. BET surface area.

Sample code	BET Surface area m^2/g
S1	153
S3	93
S4	82
S5	80
S6	66
Sulfurized S5	38

3.2. Electrochemical measurements for supercapacitors:

To demonstrate the potential application of the synthesized nanocomposites for supercapacitors, electrochemical testing was performed in 3M KOH electrolyte. The electrochemical testing was done using cyclic voltammetry, galvanostatic charge-discharge measurements and electrochemical impedance spectroscopy.

3.2.1. Cyclic voltammetry:

The cyclic voltammetry using a three electrode system was used to study the electrochemical behavior of the synthesized samples. Figures 3.32-3.37 show the CV curves of all the samples at various scan rates. It was observed that the shape of the CV curves was retained even at higher scan rates suggesting a high rate electrochemical stability of the synthesized materials.[40] Moreover, the CV curves showed a pair of redox peaks during the cathodic and anodic sweeps which confirms the presence of Faradaic redox reactions. The cyclic voltammetry was used

to calculate the charge storage capacity of the samples. The specific capacitance (C_{sp}) of the samples was calculated using the following expression:

$$C_{sp} = \frac{Q}{\Delta V.m} \qquad \ldots. (1)$$

Where Q is the area under the CV curve, ΔV is the potential window, and m is the mass of the synthesized sample used in the electrode. The variation of the specific capacitance as a function of scan rate for all the synthesized samples is shown in Figure 3.38. It was observed that specific capacitance of all the nanocomposites decreases with an increase in scan rates. Lower specific capacitance at higher scan rates could be due to lack of time for the electrolyte ions to be active on the surface of the electrode.[41] The higher specific capacitance in the nanocomposites could be due to participation of cobalt oxides in the redox reactions. The specific capacitance for all the synthesized samples at 1 mV/s of scan rate is given in Table 3.2. As seen in Table 3.2, sample S4 showed the highest specific capacitance of 1,533 F/g at 1 mV/s. The specific capacitance of polypyrrol (sample S1) and cobalt oxide (sample S6) was observed to be 439 and 582 F/g, respectively.

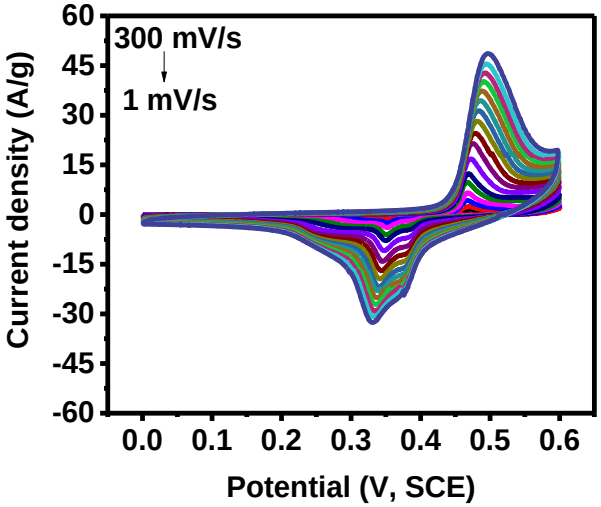

Figure 3.32. CV curves of S1 sample at various scan rates in 3M KOH electrolyte.

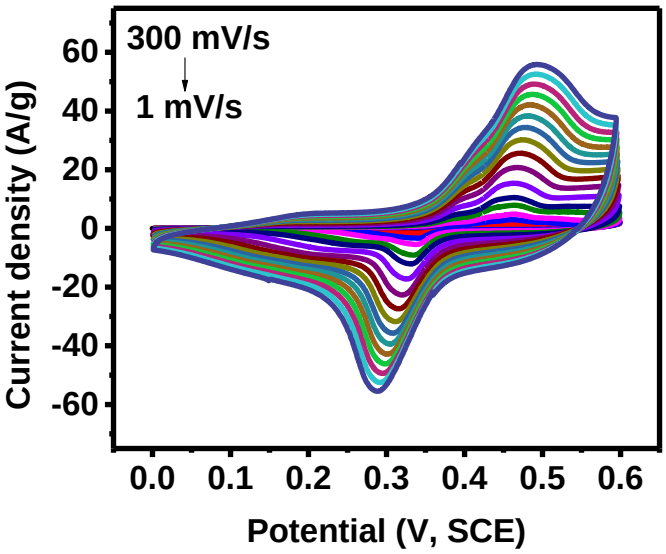

Figure 3.33. CV curves of S2 sample at various scan rates in 3M KOH electrolyte.

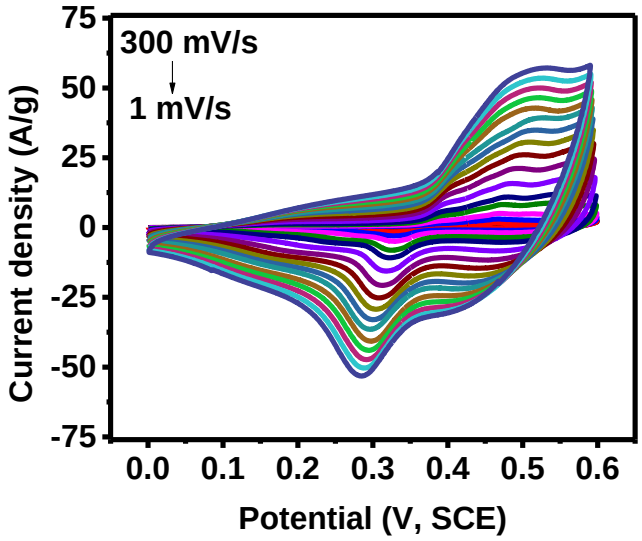

Figure 3.34. CV curves of S3 sample at various scan rates in 3M KOH electrolyte.

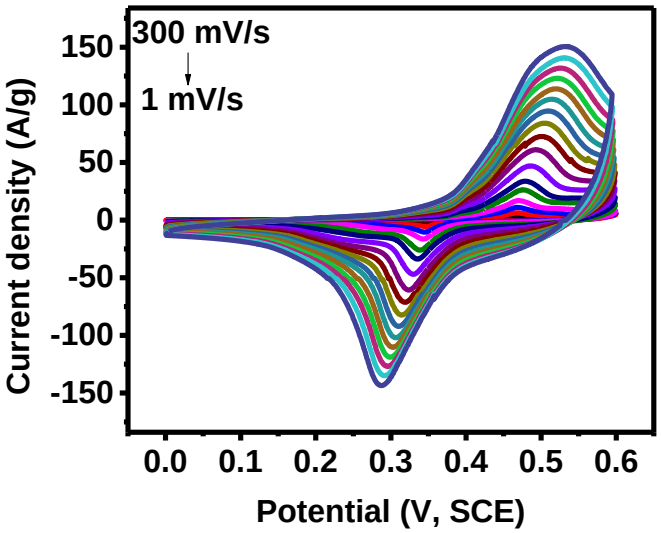

Figure 3.35. CV curves of S4 sample at various scan rates in 3M KOH electrolyte.

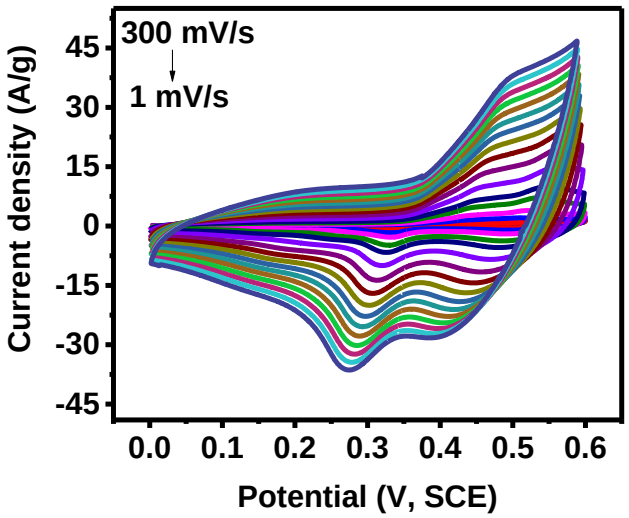

Figure 3.36. CV curves of S5 sample at various scan rates in 3M KOH electrolyte.

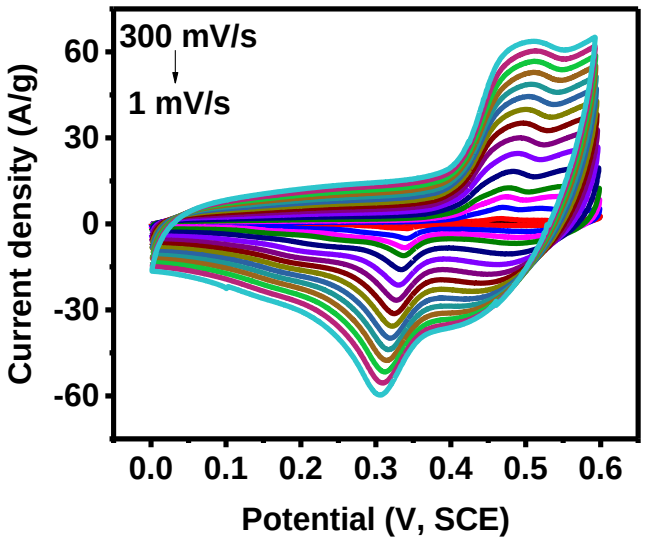

Figure 3.37. CV curves of S6 sample at various scan rates in 3M KOH electrolyte.

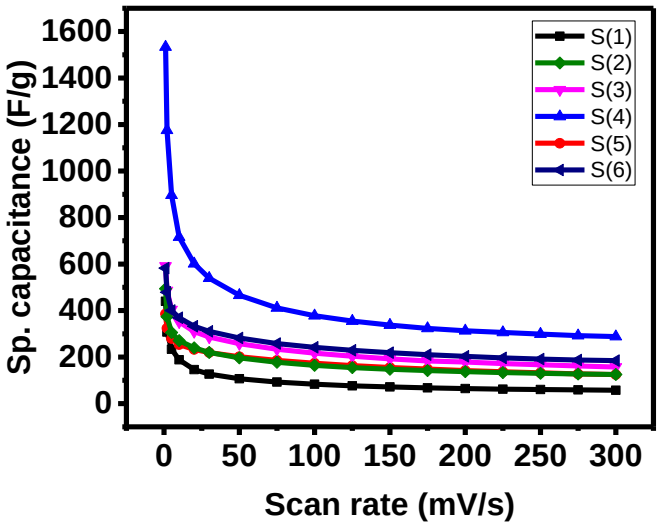

Figure 3.38. The variation of specific capacitance as a function of scan rates for all synthesized samples in 3M KOH electrolyte.

Table 3. Specific capacitance of all the synthesized samples at 1 mV/s.

Sample code	Specific capacitance (F/g)
S1	439
S2	494
S3	591
S4	1533
S5	385
S6	582

3.2.2. Galvanostatic charge-discharge studies:

The charge storage capacity of the synthesized samples was also studied using galvanostatic charge-discharge measurements at various applied current densities in the potential range of 0- 0.6 V (vs. SCE). A current density of 0.5, 0.75, 1, 1.5, 2, 3, 4, 5, 7, 10, 15, and 20 A/g was applied to study the charge-discharge characteristics of all the samples. Figures 3.39-3.44 show the charge-discharge characteristics of all the samples. As seen in these figures, the discharge time decreased with increasing current density which could be due to insufficient time for the electrolytes to perform redox reactions at the electrode/electrolyte interface. The notable plateau regions in galvanostatic charge-discharge curves further confirm the pseudocapacitive behaviors of the synthesized materials. The pseudocapacitive behaviors resulted due to charge-transfer reaction and the electrochemical adsorption-desorption process at the electrode/electrolyte interface consistent with the redox peaks in the CV curves.[11] The following equation was used to calculate the specific capacitance of the electrodes from the galvanostatic charge-discharge studies[42]:

$$C_{sp} = \frac{I.\Delta t}{m.\Delta V} \qquad \ldots. (2)$$

Where *Csp* (F/g), *I* (A), *Δt* (s), *m* (g), and *ΔV* (V) represent the specific capacitance, the applied current density, the discharge time, mass of the active material, and working potential range, respectively. The highest specific capacitance of 468 F/g (at 0.5 A/g) was observed for sample S4 which is consistent with CV measurements. Guan *et al* [43] reported a specific capacitance of 60 F/g (at 1 A/g) for the composite of the needle-like Co_3O_4/graphene. Our result showed a specific capacitance of 451 F/g (at 1 A/g) for sample S4 which is over six times better than Guan et al's report. The variations in the specific capacitance as a function of current densities are shown in Figures 3.45. It is observed that specific capacitance decreases with increasing current densities; that could be due to lack of the available time for the electrolyte ions to react with the material.[41]

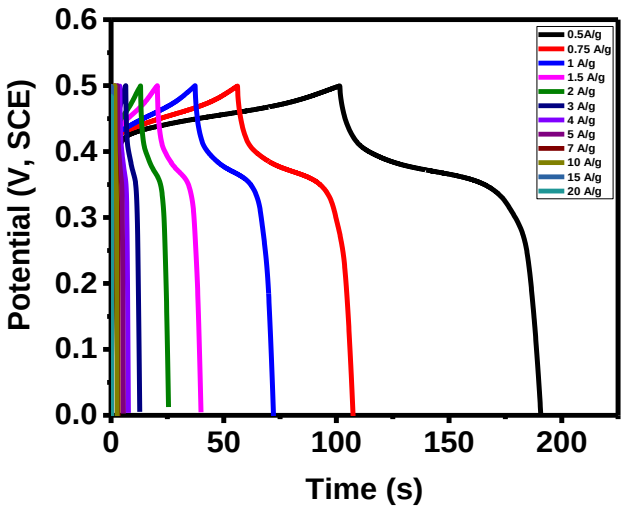

Figure 3.39. Galvanostatic charge-discharge curves of S1 sample at different current densities in 3M KOH.

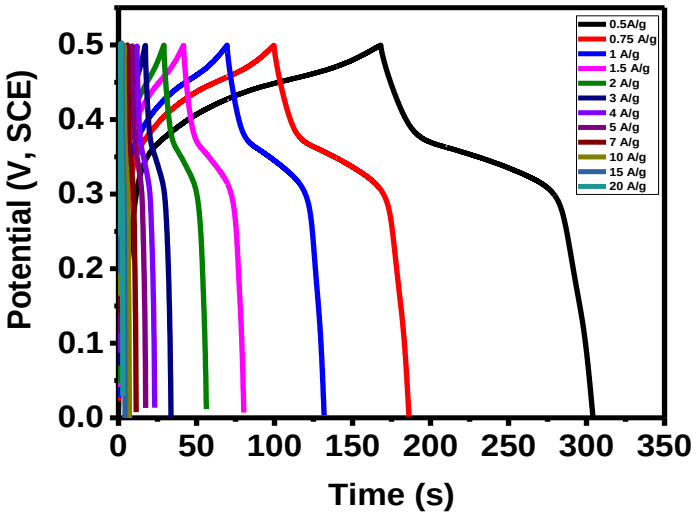

Figure 3.40. Galvanostatic charge-discharge curves of S2 sample at different current densities in 3M KOH.

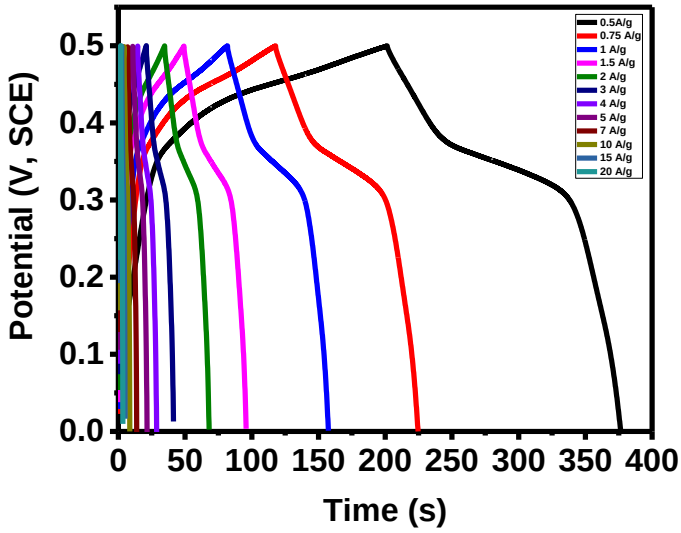

Figure 3.41. Galvanostatic charge-discharge curves of S3 sample at different current densities in 3M KOH.

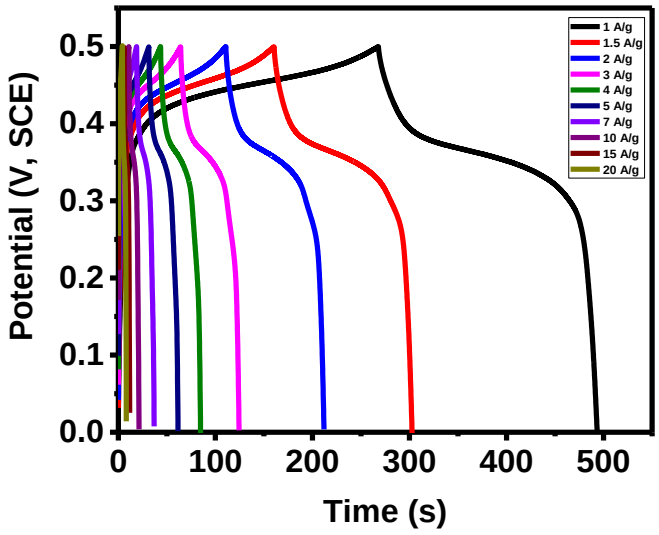

Figure 3.42. Galvanostatic charge-discharge curves of S4 sample at different current densities in 3M KOH.

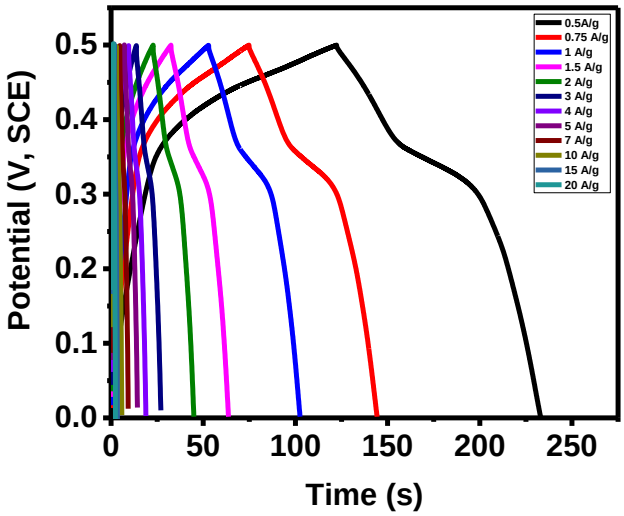

Figure 3.43. Galvanostatic charge-discharge curves of S5 sample at different current densities in 3M KOH.

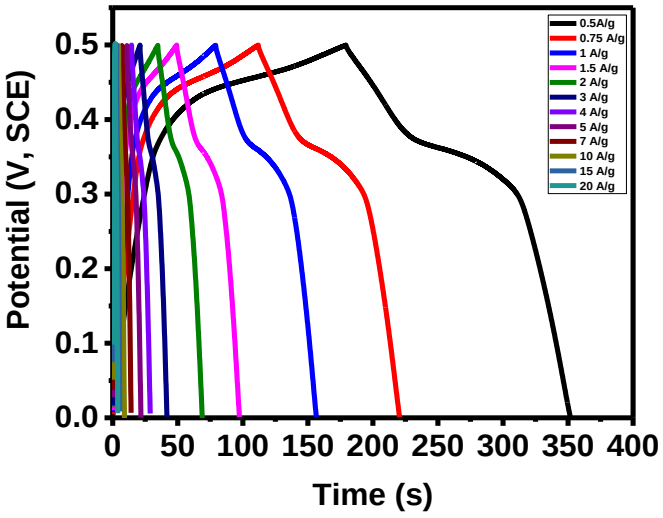

Figure 3.44. Galvanostatic charge-discharge curves of S6 sample at different current densities in 3M KOH.

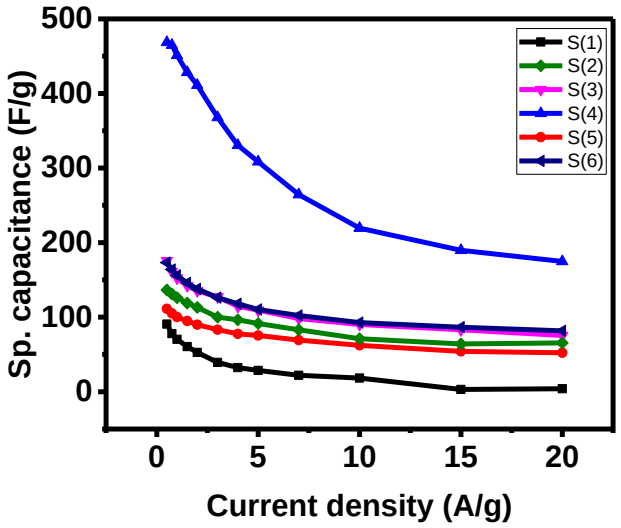

Figure 3.45. The variation of specific capacitance as a function of current density for all the synthesized samples in 3M KOH.

3.2.3. Electrochemical stability of the nanocomposite:

The electrochemical cyclic stability and Columbic efficiency of the best nanocomposite (sample S4) were studied using the cyclic galvanostatic charge-discharge method. Figure 3.46 shows the capacitance retention as a function of the number of charge-discharge cycles studied at

a current density of 4 A/g. The inset of Figure 3.46 shows the first ten and the last ten charge-discharge cycles. As seen in the plot, the electrode exhibited an exceptional cycling stability with 87% retention of its initial capacitance. On the other hand, the electrode exhibited a Columbic efficiency of 98% over 5,000 cycles of this study. The Columbic efficiency (n) was calculated using the following equation:[8]

$$n = \frac{t_D}{t_C} . 100\ \% \qquad \ldots . (3)$$

Where the t_D and t_C are the discharge and charge time in seconds.

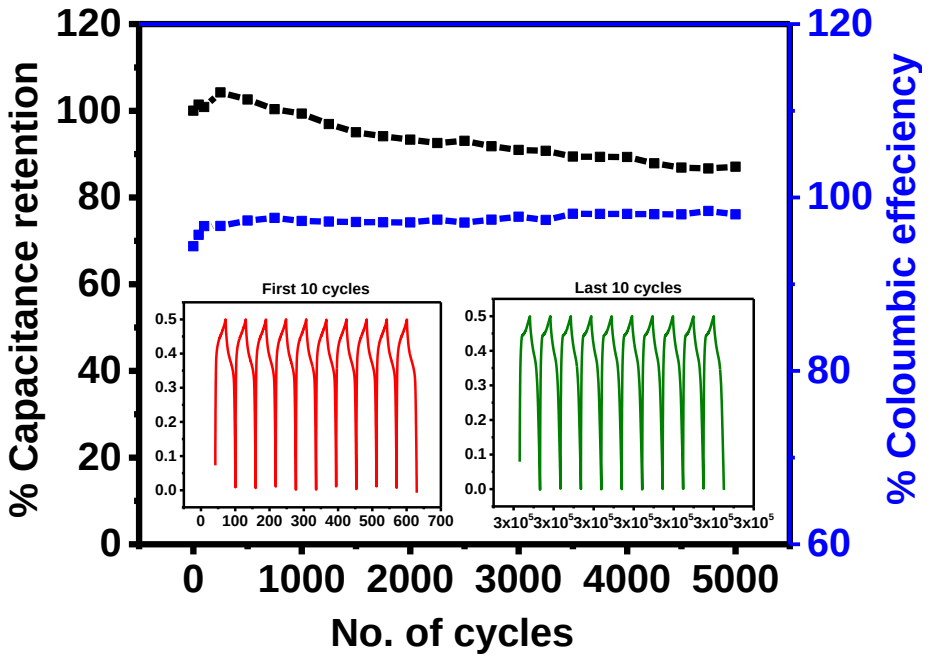

Figure 3.46. Cycling performance and Columbic efficiency of sample S4.

3.2.4. Electrochemical behavior of supercapacitor:

The symmetric supercapacitor device was fabricated using the best sample (S4) to check the potential applicability of the nanocomposite for supercapacitor applications. The electrochemical performance of the device was examined using cyclic voltammetry and galvanostatic charge-discharge measurements in 3M KOH electrolyte. Figure 3.47 shows the CV

curves of the supercapacitor device at different scan rates at room temperature. The CV curves are identical in shape even at a high scan rate, indicating high electrochemical rate stability of the device. It was further observed that specific capacitance of the supercapacitor device decreases with increasing scan rate as shown in Figure 3.48. The highest specific capacitance of 43 F/g was observed at 5 mV/s. The charge storage capacity was further analyzed using Galvanostatic charge-discharge measurements. Figure 3.49 shows charge-discharge characteristics of the device at various current densities. The variation in the specific capacitance of the device as a function of applied current is shown in Figure 3.50. The maximum charge storage capacity of 16 F/g was observed at current density of 0.3 A/g.

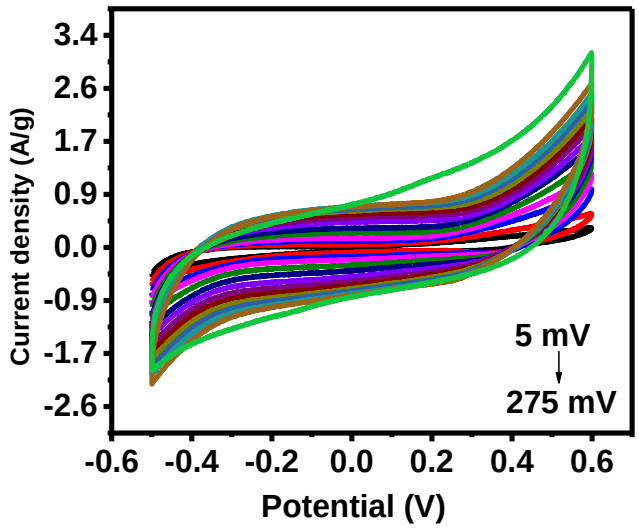

Figure 3.47. CV curves of the supercapacitor device at room temperature.

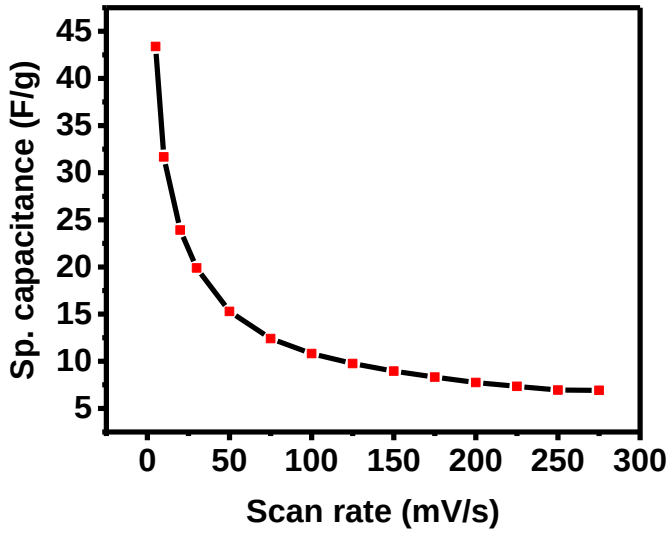

Figure 3.48. Specific capacitance of the device versus scan rate at room temperature.

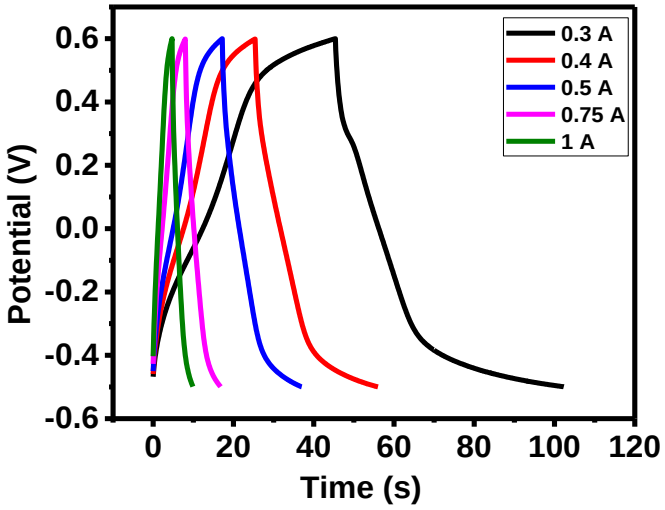

Figure 3.49. Galvanostatic charge-discharge characteristics of the supercapacitor device at room temperature.

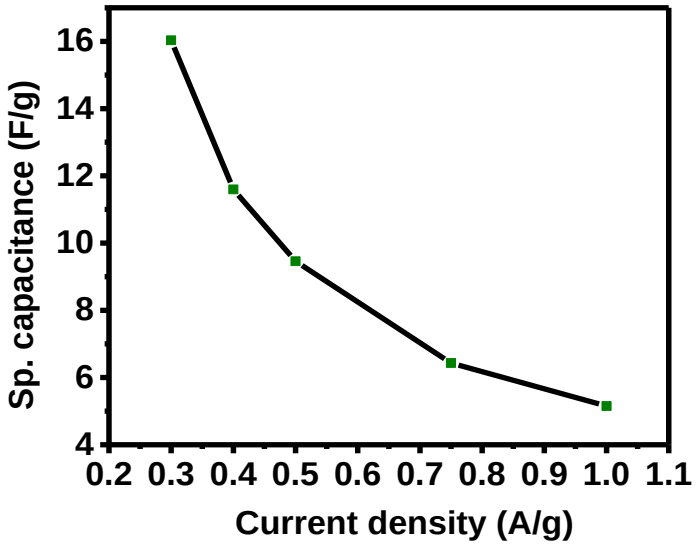

Figure 3.50. Specific capacitance of the device versus current density at room temperature.

The electrochemical properties of the supercapacitor device were studied at various temperatures to understand the effect of operating temperature on the performance of the supercapacitor device. Figure 3.51 shows the CV curves of the device at different temperatures. As seen, the shape of the CV curves are identical and the area under the curve increases with increase in temperature. Identical shapes in the CV curves even at higher temperature confirm the electrochemical stability of the device. Figure 3.52 shows the percentage change in the specific capacitance of the device with increase in temperature. About 80% improvement in the specific capacitance of the device was observed when the temperature was increased from 10 to 60 ^{o}C. The effect of temperature on the charge-discharge characteristics was also studied. The discharge time was observed to be increasing with increase in temperature as seen in Figure 3.53, which confirms the improvement in the charge storage capacity of the device at higher temperature. From the galvanostatic charge-discharge measurements, about 300% improvement in charge storage capacity of the supercapacitive device was observed on increasing temperature from 10 to 60 ^{o}C (Figure 3.54).

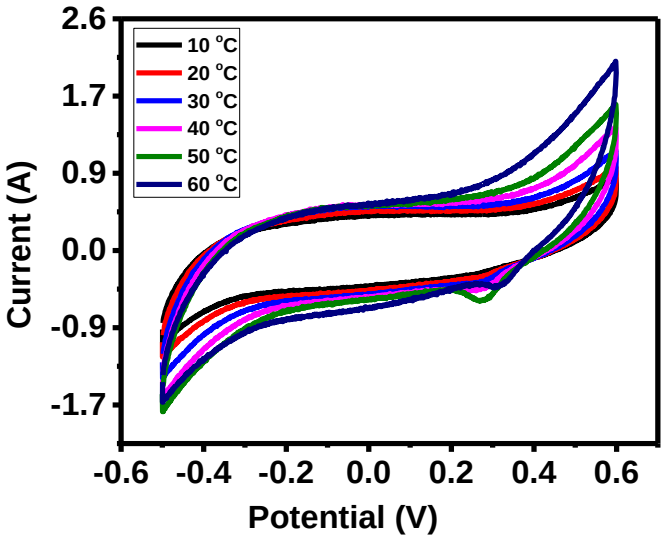

Figure 3.51. CV curves of the supercapacitor device at different temperatures.

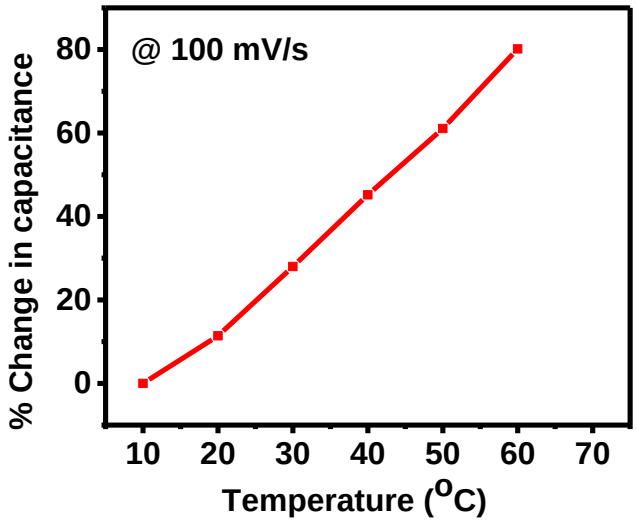

Figure 3.52. Effect of temperature on charge storage capacity of S4 device determined from CV measurements.

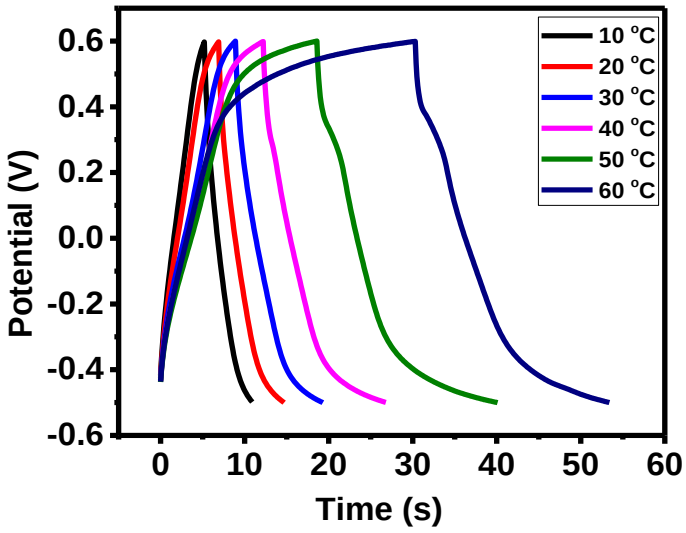

Figure 3.53. Galvanostatic charge-discharge curves of S4 device at various temperatures.

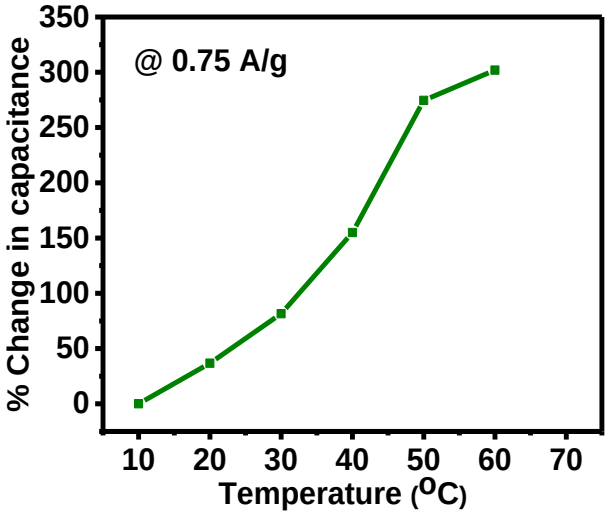

Figure 3.54. Effect of temperature on charge storage capacity of S4 device determined from GCD characteristics.

3.3. Electrochemical measurements for oxygen and hydrogen evolution reaction:

3.3.1. Oxygen evolution reaction:

The oxygen evolution reaction was studied using linear sweep voltammetry and electrochemical impedance spectroscopy. Electrocatalytic properties of all the prepared samples

were studied using the materials on nickel foam in 1M KOH electrolyte. Figure 3.55 shows the polarization curves of all the samples. It is clear from the polarization studies that sample S5 exhibited the lowest overpotential of 316 mV to achieve a current density of 10 mA/cm^2. The overpotential for all samples at a current density of 10 mA/cm^2 is shown in Table 3.3. The corresponding Tafel slopes for all the samples are shown in Figure 3.56. The Tafel slopes provide information about the kinetics of electron transfer during OER process. As observed, sample S1 shows the best Tafel slope among the studied samples.

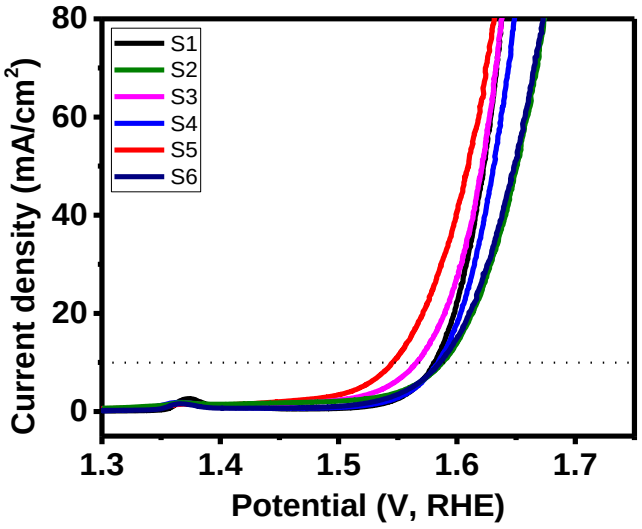

Figure 3.55. Polarization curves of all the samples.

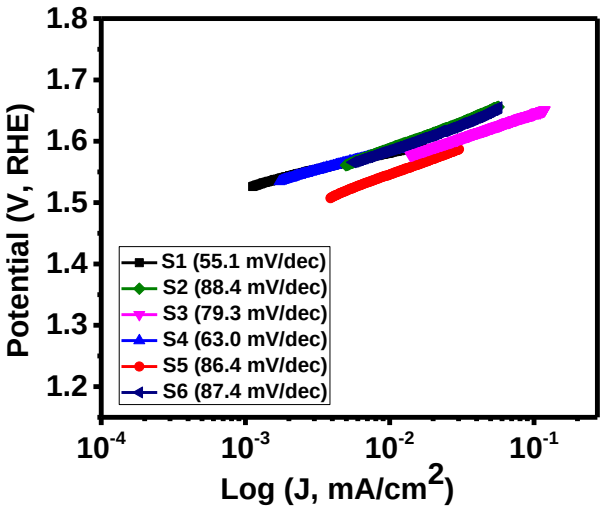

Figure 3.56. Tafel slopes for all the samples.

Table 4. OER overpotential for all samples at 10 mA/cm^2.

Sample code	Overpotential (mV)
S1	350
S2	358
S3	336
S4	354
S5	316
S6	356

Furthermore, electrochemical impedance spectroscopy was used to study the electrocatalytic activities of the synthesized samples. Figure 3.57 shows the variation of total impedances as a function of frequency (at 0.50 V vs SCE) for all the samples. It is clear from the

figure that sample S5 has the lowest impedance. The charge transport resistance of the studied samples was further investigated using Nyquist plots as shown in Figure 3.58. The charge-transport resistance which is represented by the radius of the semicircle in the high-frequency range is the lowest for sample S5, suggesting fastest electron transfer rate among the studied samples. The electrochemical impedance spectra for sample S5 were studied at various potentials (0, 0.40, 0.45, 0.50, 0.55 and 0.60V vs SCE) and shown in Figures 3.59 and Figure 3.60.

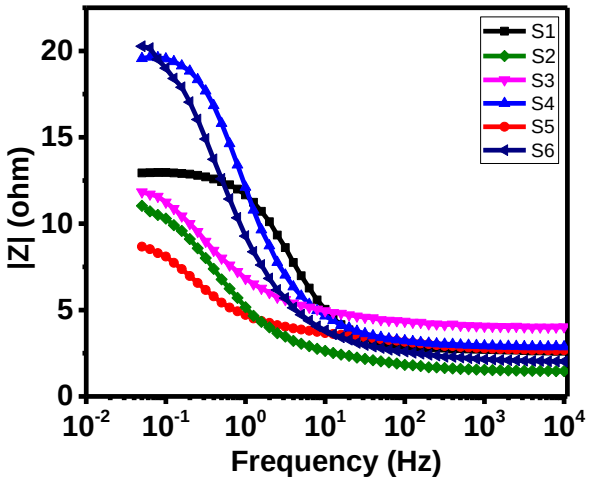

Figure 3.57. Variation of Z versus frequency for all the samples at 0.5 V vs SCE.

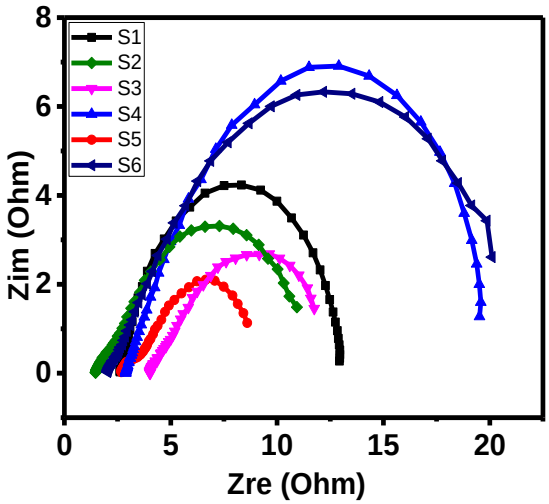

Figure 3.58. Variation Zre versus Zim for all the samples at 0.50 V vs SCE.

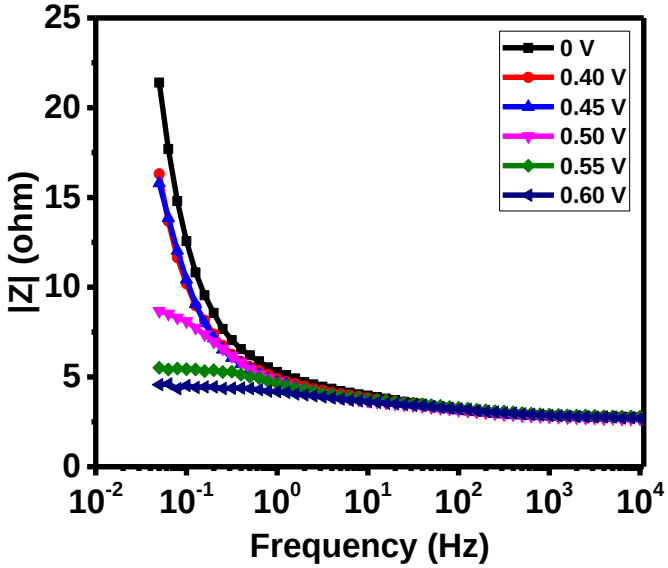

Figure 3.59. Variation of Z versus frequency for S5 sample at various voltages.

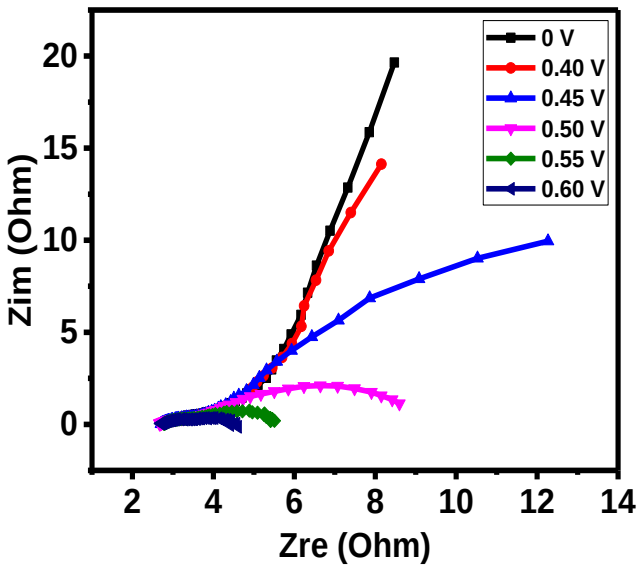

Figure 3.60. Variation Zre versus Zim for S5 sample at various voltages.

The total impedance decreases with increasing potential, confirming that resistance decreases with increase in overpotential. The diameter of the semicircle decrease with increase in potential, indicating faster electron transfer at higher overpotentials. Moreover, the electrochemical

stability of S5 as an electrocatalyst was studied using linear sweep voltammetry, electrochemical impedance spectroscopy and chronoamperometry measurments. As shown in Figure 3.61, S5 showed a very durable electrocatalytic performance up to 2,000 cycles of testing. A very slight differenc in overpotential equal to 5 mV at 10 mA/cm^2 was observed between the first and the 2,000th cycles, which confirms the electrochemical durability of the S5 sample during the polarization measurements. Figure 3.62 and Figure 3.63 show the electrochemical impedance spectroscopy measurements for sample S5 before and after 2,000 cycles of polarization study. It is clear from these figures that nanocomposite of polypyrrole and cobalt oxide is electrochemically very stable. Electrochemical stability of the S5 sample was further studied using chronoamperometric testing. The resultant chronoamperometric plot is shown in Figure 3.64. Our results suggest that the nanocomposite of polypyrrole and cobalt oxide is electrochemically very stable with low overpotential and could be used for water splitting application. [27]

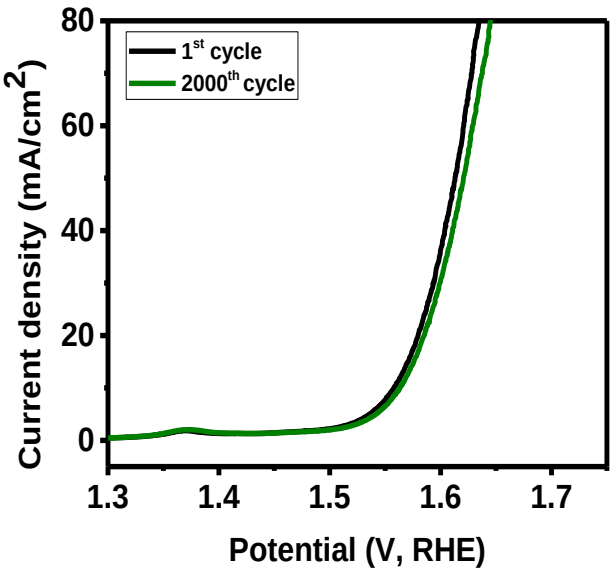

Figure 3.61. Electrochemical stability test for S5 sample using linear sweep voltammeter.

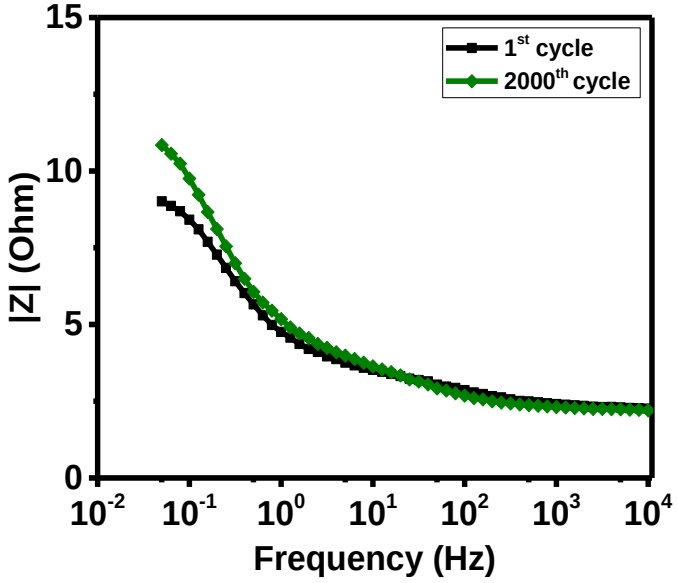

Figure 3.62. Impedance versus frequency plots for S5 sample at 0.50 V vs SCE.

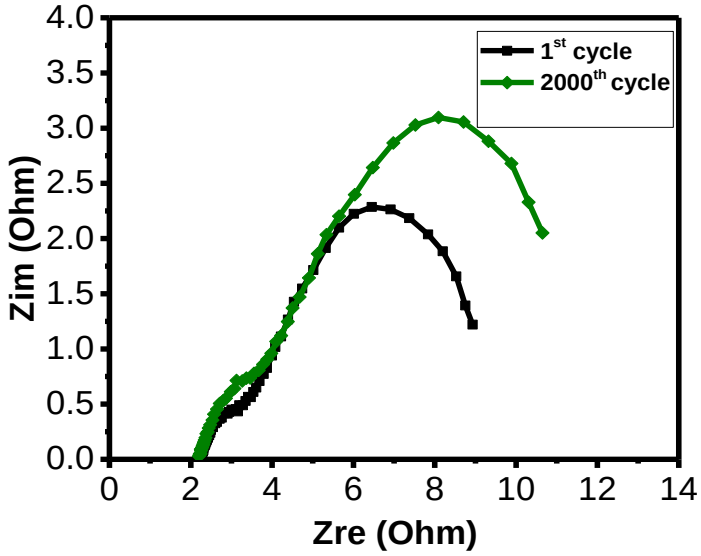

Figure 3.63. Zre versus Zim plots at 0.5 V for S5 sample before and after stability test.

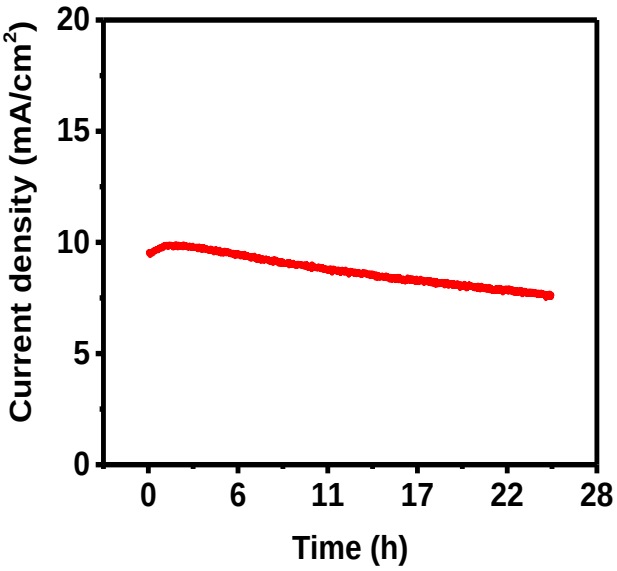

Figure 3.64. Durability test for S5 sample using chronoamperometry.

3.3.2. Hydrogen evolution reaction:

The electrocatalytic performance of the synthesized materials for hydrogen evolution reaction was also studied using linear sweep voltammetry and electrochemical impedance spectroscopy. The polarization curves for all the synthesized samples are shown in Figure 3.65. As seen in the polarization curves, sample S5 required the lowest overpotential of 132 mV to achieve a current density of 10 mA/cm^2. The overpotential for all the samples at 10 mA/cm^2 is presented in Table 3.4. The corresponding Tafel slope for all samples is shown in Figure 3.66. Even though S5 showed the lowest overpotential, it was not the fastest in kinetic reaction.

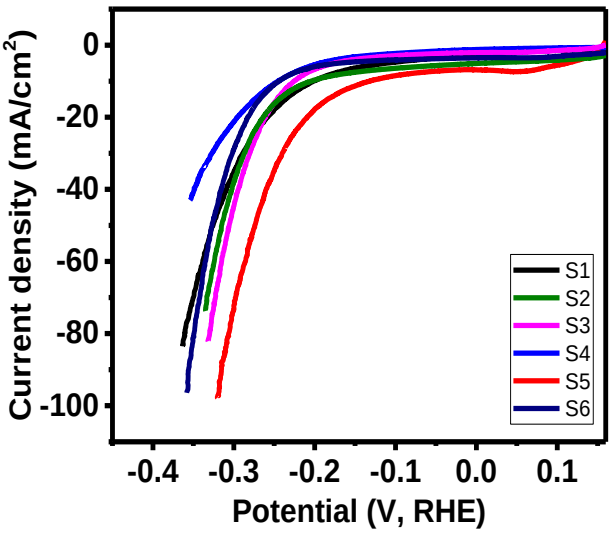

Figure 3.65. Polarization curves of all the samples.

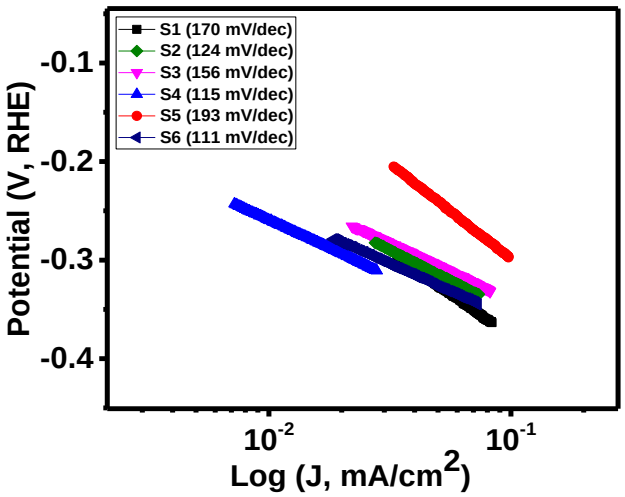

Figure 3.66. Tafel plots for all the samples.

Table 5. HER overpotential required for all the samples to achieve a current density of 10 mA/cm2.

Sample code	Overpotential (mV)
S1	201
S2	204
S3	225
S4	259
S5	132
S6	243

The electrochemical impedance spectroscopy measurements were used to analyze the HER activity and the electrical conducting behavior of the samples at -1.25 V vs SCE. The variation in the impedance of the samples as a function of frequency is shown in Figure 3.67. As seen in the figure, S5 displayed the lowest impedance which resulted in high electro-catalytic activity because of the lower charge transfer resistance.[44] The Nyquist plots for all the samples are displayed in Figure 3.68. As seen in the Nyquist plots, sample S5 showed the lowest charge-transport resistance (smallest diameter), which resulted in the faster electron transfer rate. The electrochemical impedance spectroscopy measurements for sample S5 were investigated at various potentials (1.1, 1.15, 1.2, 1.25, 1.30 and 1.35 V vs SCE) and shown in Figures 3.69 and Figure 3.70. As seen in both figures, the total impedance of sample S5 decreases with increasing potential. Figure 3.71 shows the electrochemical stability performance of S5 electrocatalyst for HER using linear sweep voltammeter. A slight increase in the overpotential was observed after 2,000 cycles of polarization.

The result of chronoamperometric testing is shown in Figure 3.72. A very small loss in current density was observed indicating electrochemical stability of the sample.

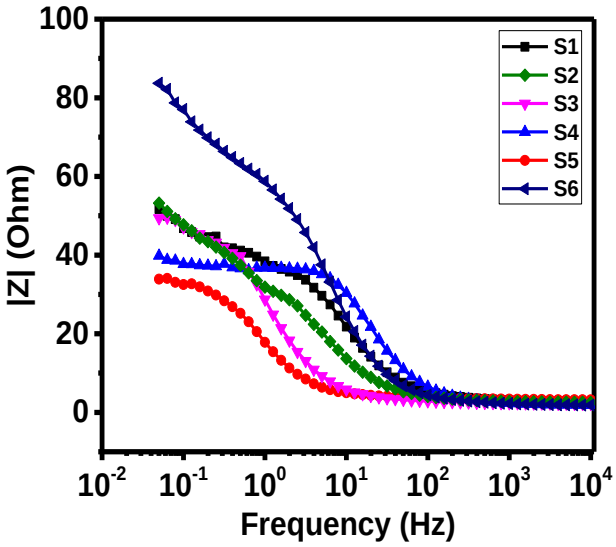

Figure 3.67. Variation of Z versus frequency for all the samples measured at -1.25 V vs SCE.

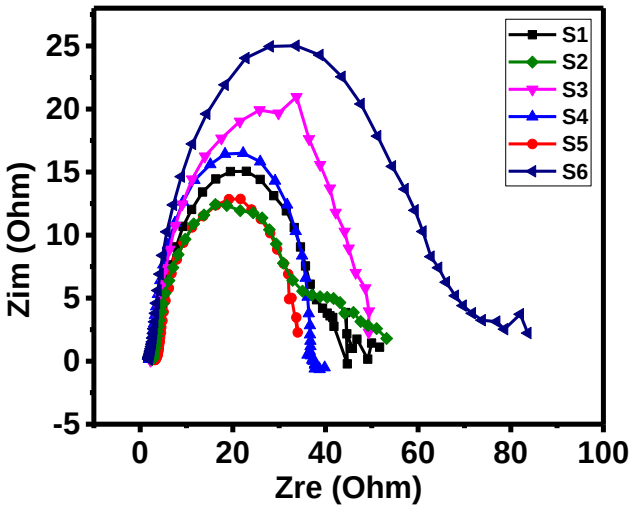

Figure 3.68. Nyquist plots for all the samples at -1.25 V vs SCE.

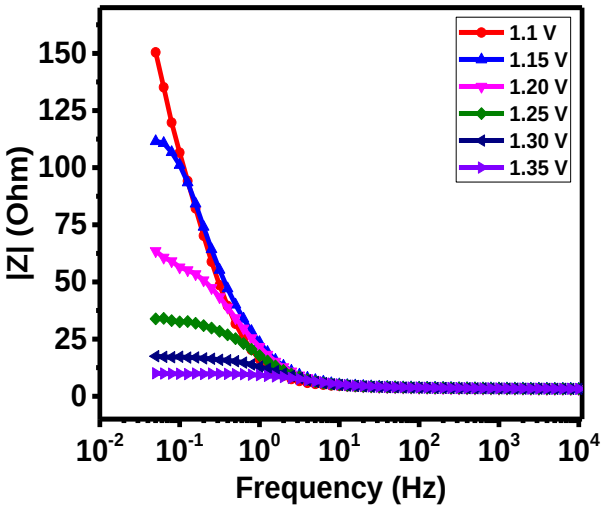

Figure 3.69. Variation of Z versus frequency for S5 sample at various potentials.

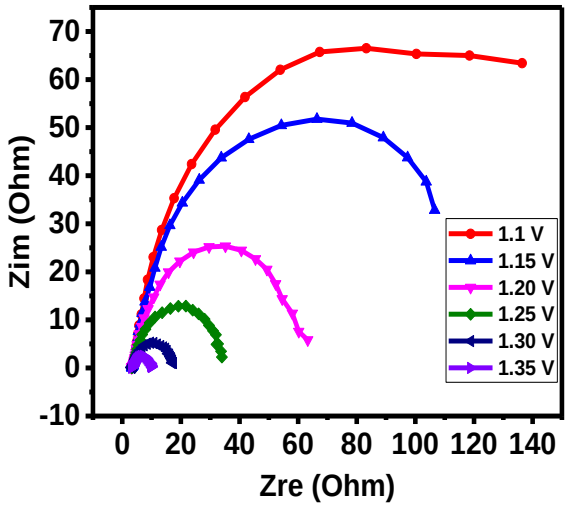

Figure 3.70. Variation Zre versus Zim for S5 sample at various potentials.

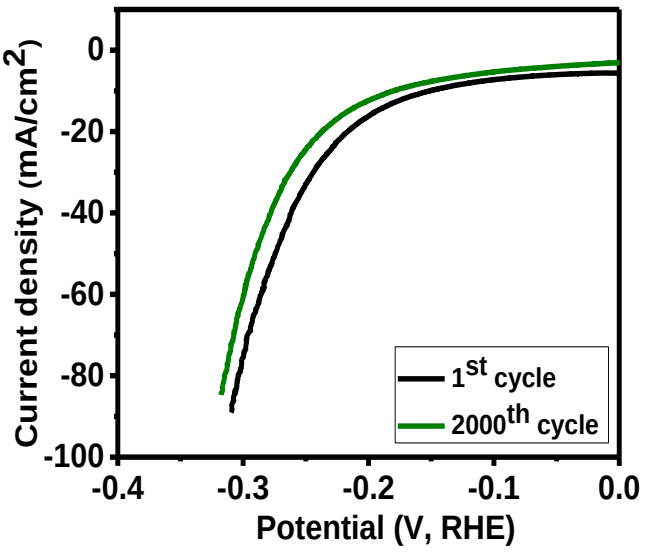

Figure 3.71. Stability test of S5 electrocatalyst using linear sweep voltammeter.

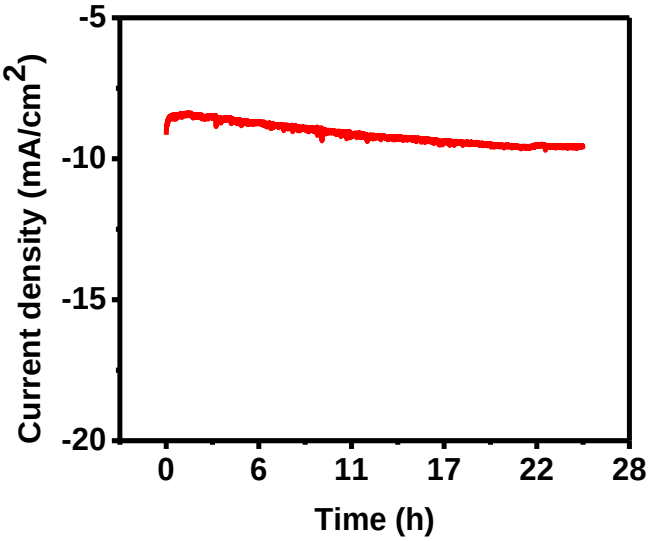

Figure 3.72. Durability test of S5 electrocatalyst using chronoamperometry.

3.4. Electrochemical measurements sulfurized nanocomposites:

The electrochemical properties of metal oxides could be improved by sulfuring them. Transition metal sulfides have better electronic conductivity compared with their oxides. Higher electronic conductivity reduces the sheet and charge transfer resistance of the electrodes and thus improves electrochemical properties. We sulfurized the best sample (S5) to see the effect of sulfurization on electrocatalytic properties of nanocomposite.

3.4.1. Oxygen evolution studies:

The linear sweep voltammetry was employed to study the oxygen evolution reaction of sulfurized sample in 1M KOH electrolyte. Figure 3.73 shows the polarization curves of S5 and sulfurized S5 samples for comparison. A significant reduction in overpotential after sulfurization was observed. The sulfurized S5 sample required 293 mV to achieve a current density of 10 mA/cm^2, while S5 required an overpotential of 316 mV. There was a reduction in overpotential by 23 mV after sulfurization. Furthermore, the Tafel slope was also improved. The Tafel slope improved from 116 to 89 mV/dec after sulfurization (Figure 3.74). The lower Tafel slope after sulfurization indicates better OER kinetics and faster electron transfer.

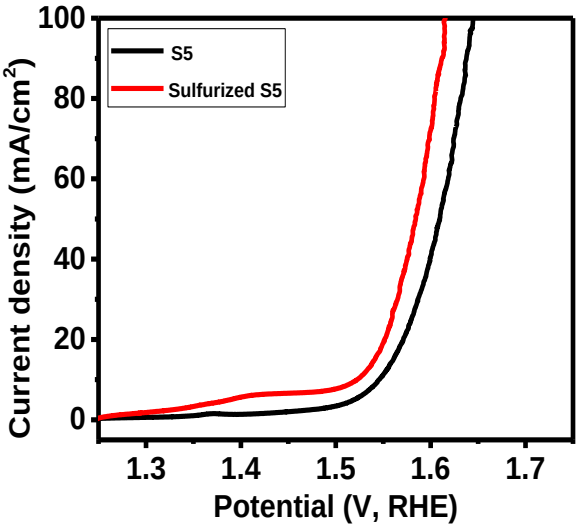

Figure 3.73. Polarization curves of S5 and sulfurized S5 samples.

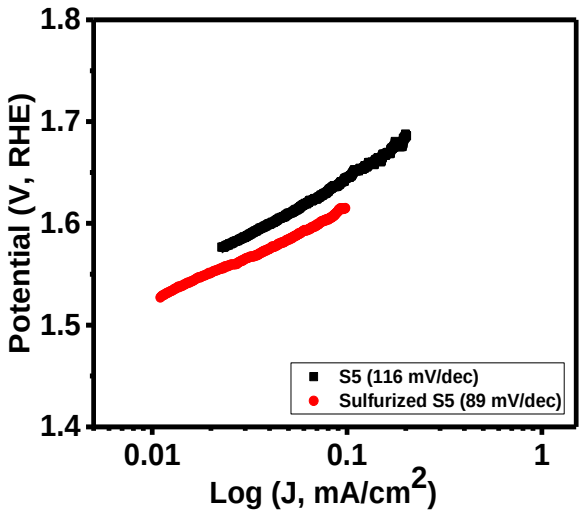

Figure 3.74. Tafel plots and slopes of S5 and sulfurized S5 samples.

The effect of sulfurization on impedance properties of the S5 sample was also investigated using electrochemical impedance spectroscopy. Figure 3.75 shows the variation of impedance versus frequency for S5 and sulfurized S5 samples at 0.50 V vs SCE. It is clear from the graphs that the sulfurized S5 sample has lower impedance compared to S5. The charge transport resistance of these samples was further analyzed using Nyquist plots (Figure 3.76). The charge-transfer resistance, represented by the diameter of the semicircle in high frequency range, is significantly reduced after sulfurization of sample S5. Figure 3.77 and Figure 3.78 show the impedance studies for the sulfurized S5 sample at various potential. It was observed that impedance and charge-transfer resistance decreases with increasing potential.

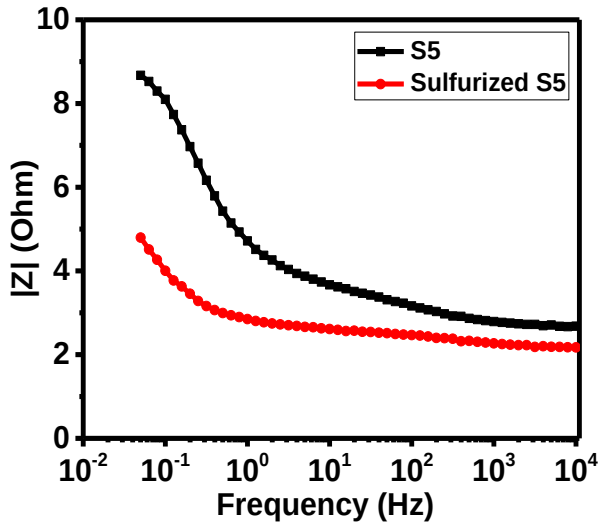

Figure 3.75. Variation of Z versus frequency for S5 and sulfurized S5 at 0.50 V vs SCE.

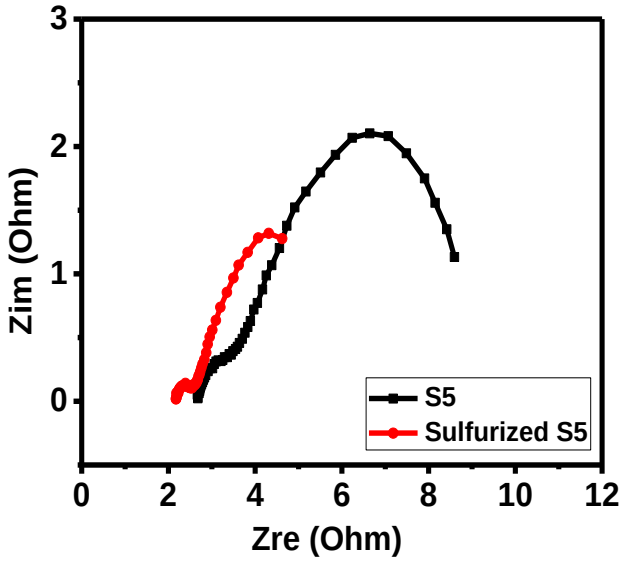

Figure 3.76. Variation Zre versus Zim for S5 and sulfurized S5 at 0.50 V vs SCE.

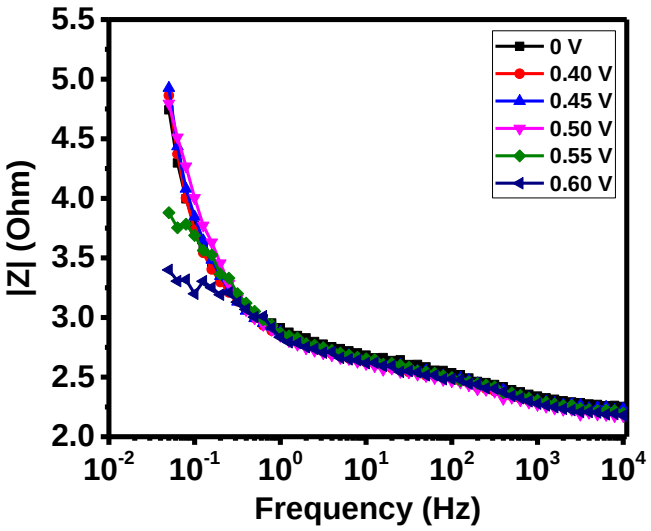

Figure 3.77. Variation of Z versus frequency for sulfurized S5 sample at various potentials.

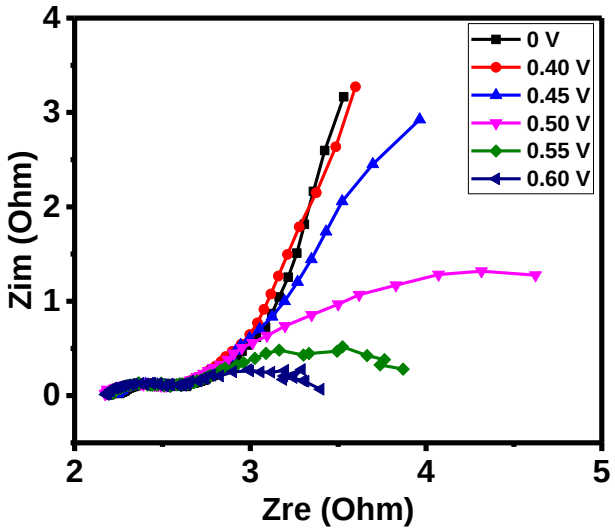

Figure 3.78. Variation Zre versus Zim for sulfurized S5 sample at various potentials.

Furthermore, the electrochemical stability of sulfurized S5 sample was studied using linear sweep voltammetry, electrochemical impedance spectroscopy and chronoamperometry mesurments. The linear sweep voltammetry measurements of sulfurized S5 were investigated up

to 2,000 cycles as shown in Figure 3.79. The 1st and 2,000th cycles overlap each other, indicating that sulfurized S5 has a high durable electrocatalytic performance up to 2,000 cycles of testing. Figure 3.80 and Figure 3.81 represent the electrochemical impedance spectroscopy stability studies of the sulfurized S5 sample. It is clear from both graphs that impedance and resistance are constant even after 2,000 cycles, which confirms the stable performance of the sample after sulfurization. In continuous electrolysis measurement, a slight decrease in current density during more than 12 hours was observed as shown in Figure 3.82, indicating chronoamerometic stability of the sulfurized sample.

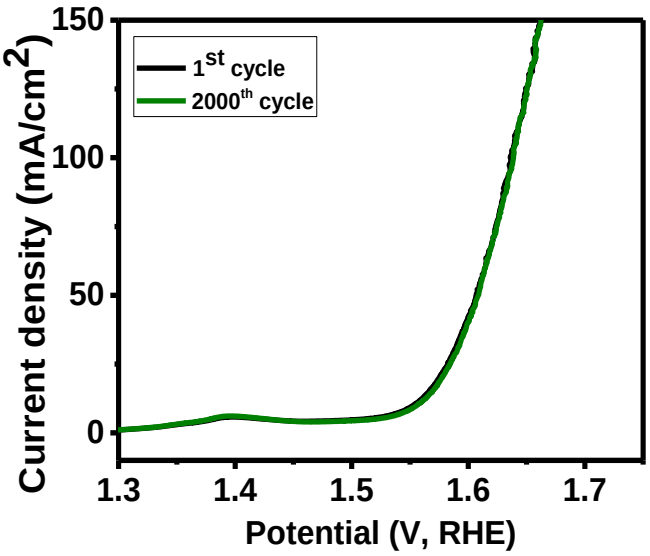

Figure 3.79. Polarization curves of sulfurized sample at different cycles of linear sweep voltammetry measurements.

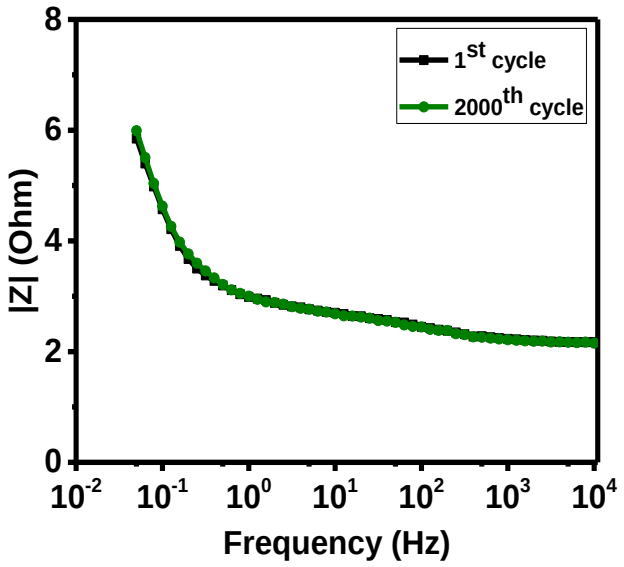

Figure 3.80. Impedance versus frequency plots for sulfurized sample before and after cyclic studies.

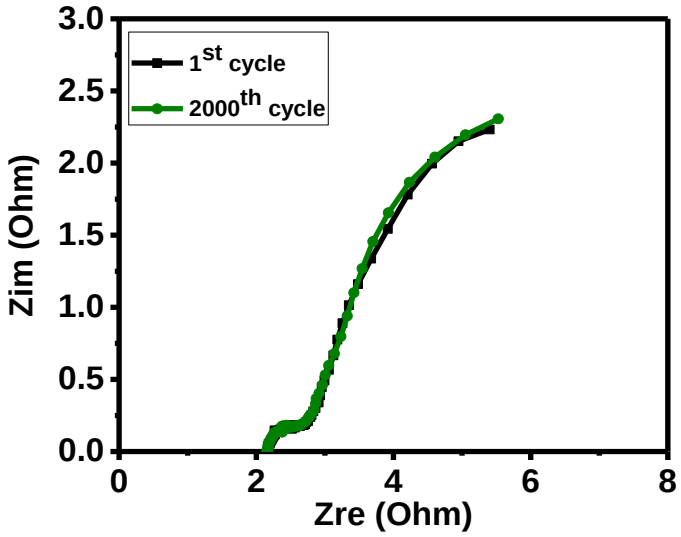

Figure 3.81. Zre versus Zim plots for sulfurized sample before and after cyclic studies.

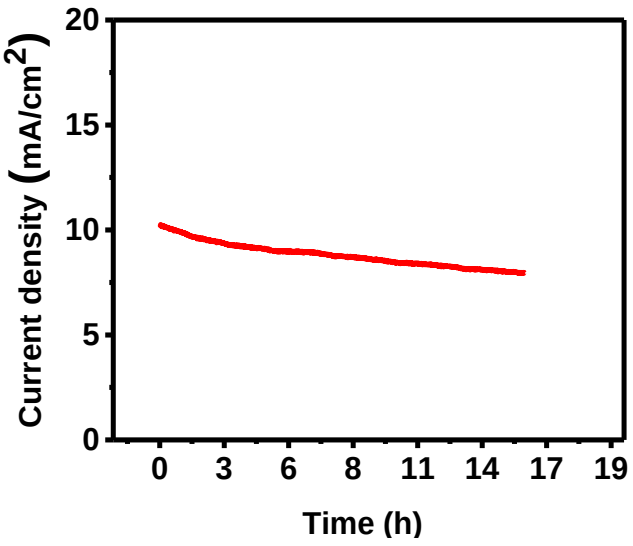

Figure 3.82. Electrochemical stability performance of sulfurized sample studied using chronoamperometry.

3.4.2. Hydrogen evolution studies:

The effect of sulfurization of HER activity was also studied. Figure 3.83 shows the polarization curves of S5 and sulfurized S5 samples. Significant improvement in HER activity in terms of overpotential after sulfurization was not observed. However, a significant improvement in the Tafel slope was observed. The Tafel slope improved from 166 to 133 mV/dec after sulfurization (Figure 3.84). That indicated a faster electron transfer process after sulfurization.

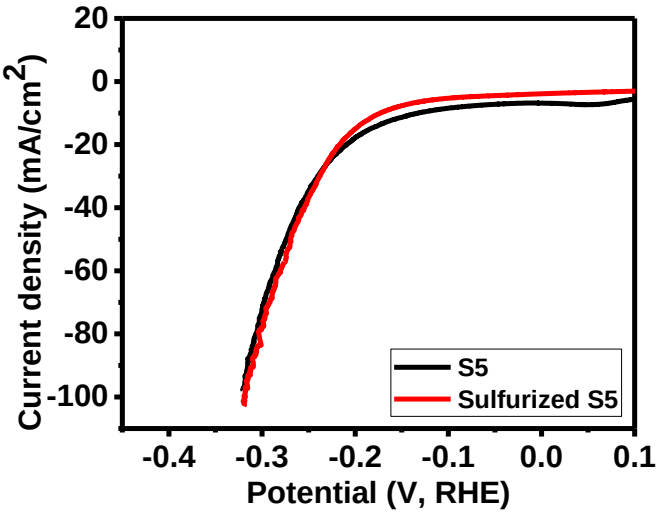

Figure 3.83. Polarization curves of S5 and sulfurized S5 samples.

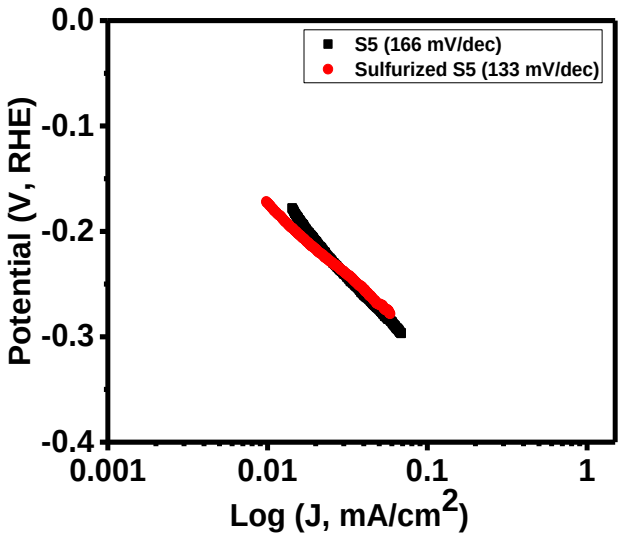

Figure 3.84. Tafel plots and slopes of S5 and sulfurized S5 samples.

Figures 3.85 and Figure 3.86 represent the electrochemical impedance studies of the HER process of sample S5 and sulfurized S5 at -1.25 V vs SCE. As seen in both figures, the sulfurized sample has lower impedance than the unsulfurized. Figure 3.87 shows variation of impedance

versus frequency of sulfurized sample in HER region at different potentials. As seen, the impedance decreases with increasing potential. Figure 3.88 represents Nyquist plots for the sulfurized sample at various potentials. It is observed that the charge-transfer resistance decreases with an increase in potential. The linear sweep voltammetry stability of the sulfurized sample is shown in Figure 3.89. It is clear from this study that the sulfurized sample is quite stable in the HER process too. The charge transfer resistance before and after the stability test was observed to be very similar (Figure 3.90 and Figure 3.91). There is clear improvement in impedance. Finally, the durability test of the sulfurized sample for the HER process was studied using chronoamperometry (Figure 3.92). The sample showed a very stable performance over 16 hours of continuous electrolysis process.

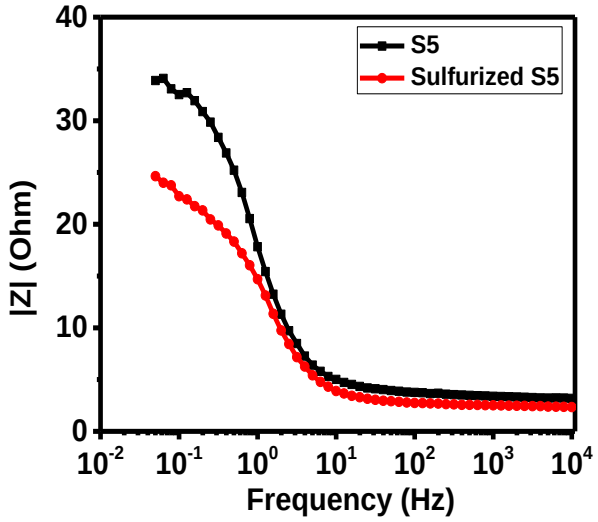

Figure 3.85. Variation of Z versus frequency for S5 and sulfurized S5 sample at -1.25 V vs SCE.

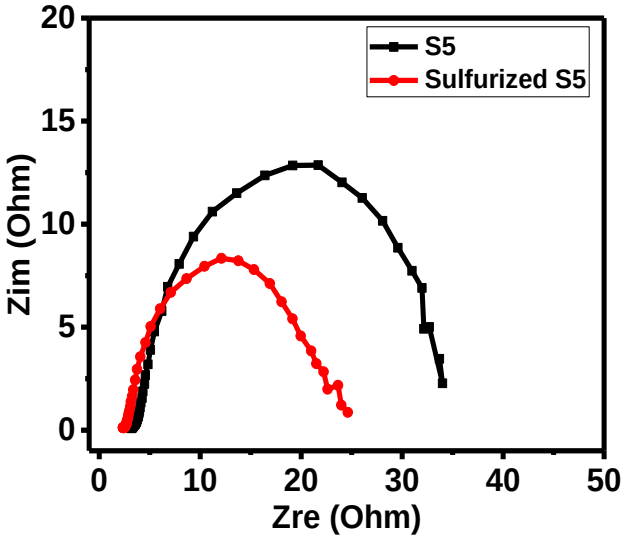

Figure 3.86. Variation Zre versus Zim for S5 and sulfurized S5 sample at -1.25 V vs SCE.

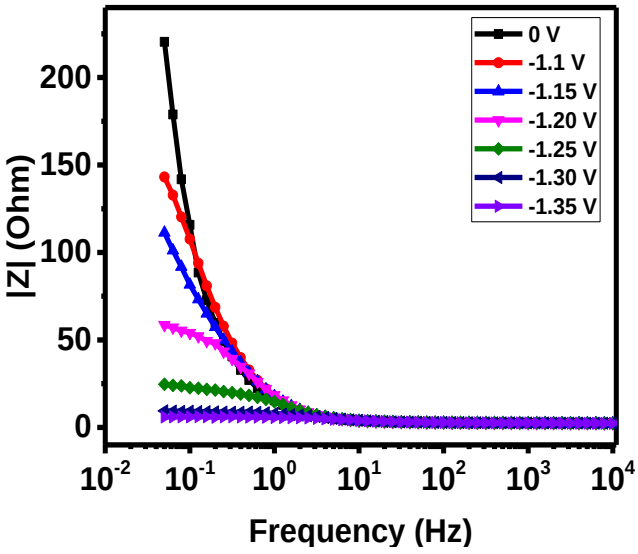

Figure 3.87. Variation of Z versus frequency for sulfurized sample at various potentials.

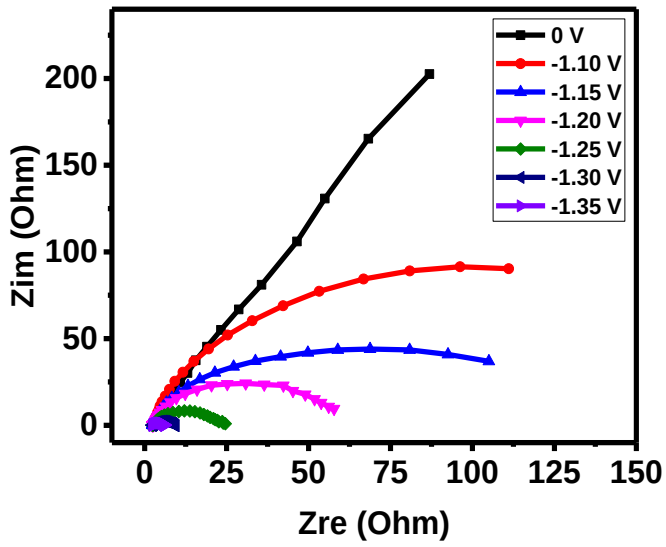

Figure 3.88. Variation Zre versus Zim for sulfurized sample at various potentials.

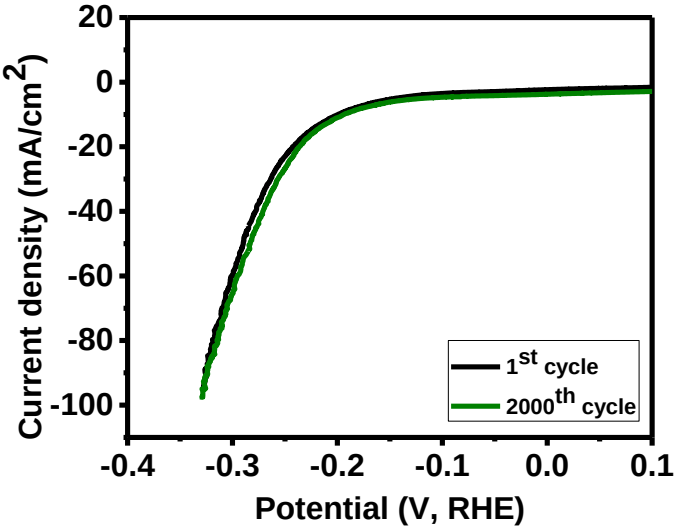

Figure 3.89. Polarization curves of sulfurized sample at different cycles of linear sweep voltammeter measurements.

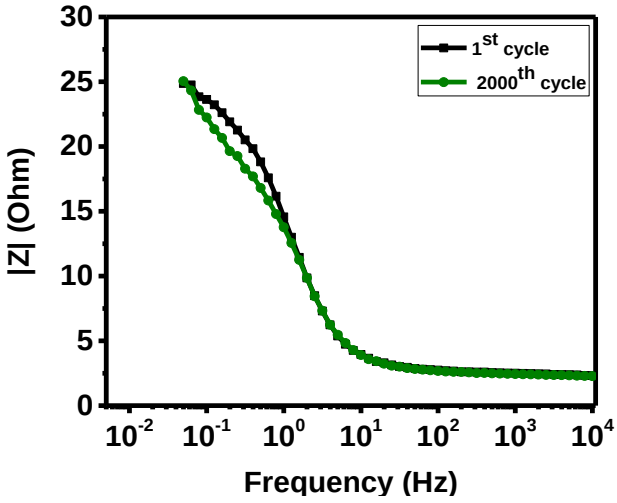

Figure 3.90. Impedance versus frequency plots for sulfurized sample before and after cyclic studies.

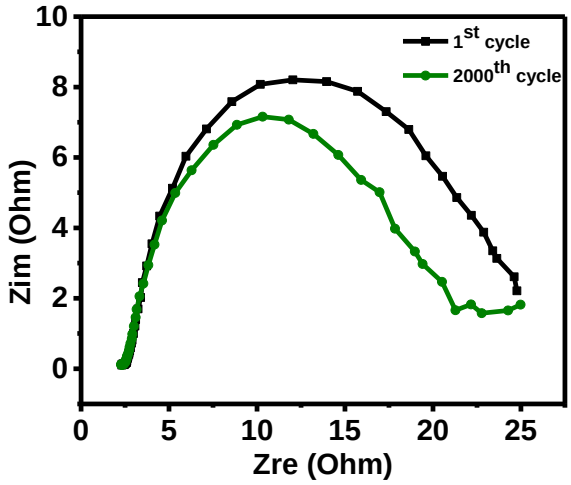

Figure 3.91. Zre versus Zim plots for sulfurized sample before and after cyclic studies.

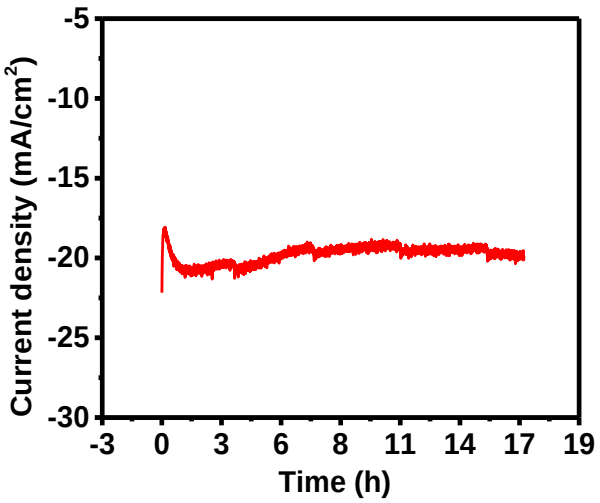

Figure 3.92. Electrochemical stability performance of sulfurized sample studied using chronoamperometry.

CHAPTER IV

CONCLUSION

In conclusion, polypyrrole was successfully synthesized by chemical polymerization. The nanocomposites of cobalt oxide and polypyrrole were synthesized using a hydrothermal method. The synthesized nanocomposites and its components were characterized using different techniques such as x-ray diffraction for phase purity, scanning electron microscopy for microstructure and morphology, the Brunauer-Emmett-Teller method for surface area, and x-ray photoelectron spectroscopy for elemental composition. Electrochemical measurements were performed in three electrodes system using cyclic voltammetry, galvanostatic charge-discharge, and electrochemical impedance spectroscopy measurements. Electrochemical measurements were performed to understand the charge storage capacity of the nanocomposites and their ability to perform as electrocatalysts for water splitting applications.

The nanocomposites showed a hybrid behavior in charge storage mechanism. The contribution from double-layer capacitance and pseudocapacitance made nanocomposites superior to their counterparts. The optimized nanocomposite showed the maximum capacitance of 1533 F/g at 1 mV/s with outstanding cycle stability. About 87% of the initial capacitance was retained after 5,000 cycles of continuous charging-discharging studies. A supercapacitor device fabricated using the best nanocomposite showed 300% improvement in charge storage capacity on increasing device temperature from 10 to 60 ^{o}C. Our results clearly suggest that nanocomposites of conducting polymer and metal oxide could be used as electrode material for fabrication of high-performance supercapacitor devices.

The potential application of these nanocomposites for water splitting was also investigated in an alkaline medium. It was observed that the nanocomposites were good electrocatalysts for water splitting compared to their counterparts as they required very low overpotential to generate hydrogen and oxygen from water. The optimized nanocomposite required 316 and 132 mV to achieve a current density of 10 mA/cm^2 for oxygen evolution and hydrogen evolution reactions, respectively. Chronoamperometric measurements confirmed their electrochemical stability as an electrocatalyst for oxygen and hydrogen evolution reactions. Furthermore, the sulfurization of S5 showed a clear and stable improvement in performing as electrolysis for oxygen and hydrogen evolution reactions. Our results suggest that optimized nanocomposites of polypyrrole and cobalt oxide could be suitable materials for energy storage as well as energy generation via water splitting.

References

(1) IBRAHIM, H.; ILINCA, A.; PERRON, J. Energy Storage systems—Characteristics and Comparisons. *Renew. Sustain. Energy Rev.* **2008**, *12*, 1221.

(2) Jaber, S. Environmental Impacts of Wind Energy. *J. Clean Energy Technol.* **2014**, *1*, 251.

(3) Mccormack, M. Renewable Energy's Future. *ACS Chemical & Engereening News*. 1999, p 20036.

(4) Kim, B. K.; Sy, S.; Yu, A.; Zhang, J. Electrochemical Supercapacitors for Energy Storage and Conversion. In *Handbook of Clean Energy Systems*; John Wiley & Sons, Ltd: Chichester, UK, 2015; p 1.

(5) Zhang, L. L.; Zhao, X. S. Carbon-Based Materials as Supercapacitor Electrodes. *Chem. Soc. Rev.* **2009**, *38*, 2520.

(6) Yu, D.; Goh, K.; Wang, H.; Wei, L.; Jiang, W.; Zhang, Q.; Dai, L.; Chen, Y. Scalable Synthesis of Hierarchically Structured Carbon Nanotube–graphene Fibres for Capacitive Energy Storage. *Nat. Nanotechnol.* **2014**, *9*, 555.

(7) Lukatskaya, M. R.; Mashtalir, O.; Ren, C. E.; Dall'Agnese, Y.; Rozier, P.; Taberna, P. L.; Naguib, M.; Simon, P.; Barsoum, M. W.; Gogotsi, Y. Cation Intercalation and High Volumetric Capacitance of Two-Dimensional Titanium Carbide. *Science (80-.).* **2013**, *341*, 1502.

(8) Rajkumar, M.; Hsu, C.-T.; Wu, T.-H.; Chen, M.-G.; Hu, C.-C. Advanced Materials for Aqueous Supercapacitors in the Asymmetric Design. *Prog. Nat. Sci. Mater. Int.* **2015**, *25*, 527.

(9) Zhou, C.; Zhang, Y.; Li, Y.; Liu, J. Construction of High-Capacitance 3D CoO@Polypyrrole Nanowire Array Electrode for Aqueous Asymmetric Supercapacitor. *Nano Lett.* **2013**, *13*, 2078.

(10) Liu, R.; Ma, L.; Huang, S.; Mei, J.; Li, E.; Yuan, G. Large Areal Mass and High Scalable and Flexible Cobalt Oxide/Graphene/Bacterial Cellulose Electrode for Supercapacitors. *J. Phys. Chem. C* **2016**, *120*, 28480.

(11) Hu, W.; Chen, R.; Xie, W.; Zou, L.; Qin, N.; Bao, D. CoNi 2 S 4 Nanosheet Arrays Supported on Nickel Foams with Ultrahigh Capacitance for Aqueous Asymmetric Supercapacitor Applications. *ACS Appl. Mater. Interfaces* **2014**, *6*, 19318.

(12) Salunkhe, R. R.; Kaneti, Y. V.; Yamauchi, Y. Metal–Organic Framework-Derived Nanoporous Metal Oxides toward Supercapacitor Applications: Progress and Prospects. *ACS Nano* **2017**, *11*, 5293.

(13) Bryan, A. M.; Santino, L. M.; Lu, Y.; Acharya, S.; D'Arcy, J. M. Conducting Polymers for Pseudocapacitive Energy Storage. *Chem. Mater.* **2016**, *28*, 5989.

(14) Shown, I.; Ganguly, A.; Chen, L.-C.; Chen, K.-H. Conducting Polymer-Based Flexible Supercapacitor. *Energy Sci. Eng.* **2015**, *3*, 2.

(15) Luo, J.; Im, J.-H.; Mayer, M. T.; Schreier, M.; Nazeeruddin, M. K.; Park, N.-G.; Tilley, S. D.; Fan, H. J.; Gratzel, M. Water Photolysis at 12.3% Efficiency via Perovskite

Photovoltaics and Earth-Abundant Catalysts. *Science (80-.).* **2014**, *345*, 1593.

(16) Wang, J.; Gao, Y.; Chen, D.; Liu, J.; Zhang, Z.; Shao, Z.; Ciucci, F. Water Splitting with an Enhanced Bifunctional Double Perovskite. *ACS Catal.* **2018**, *8*, 364.

(17) Fang, M.; Dong, G.; Wei, R.; Ho, J. C. Hierarchical Nanostructures: Design for Sustainable Water Splitting. *Adv. Energy Mater.* **2017**, *7*, 1700559.

(18) Chen, Z.; Kang, Q.; Cao, G.; Xu, N.; Dai, H.; Wang, P. Study of Cobalt Boride-Derived Electrocatalysts for Overall Water Splitting. *Int. J. Hydrogen Energy* **2018**, *43*, 6076.

(19) Licht, S.; Liu, S.; Cui, B.; Lau, J.; Hu, L.; Stuart, J.; Wang, B.; El-Ghazawi, O.; Li, F.-F. Comparison of Alternative Molten Electrolytes for Water Splitting to Generate Hydrogen Fuel. *J. Electrochem. Soc.* **2016**, *163*, F1162.

(20) Xiao, X.; Huang, D.; Fu, Y.; Wen, M.; Jiang, X.; Lv, X.; Li, M.; Gao, L.; Liu, S.; Wang, M.; et al. Engineering NiS/Ni 2 P Heterostructures for Efficient Electrocatalytic Water Splitting. *ACS Appl. Mater. Interfaces* **2018**, *10*, 4689.

(21) Wang, J.; Zhong, H.; Wang, Z.; Meng, F.; Zhang, X. Integrated Three-Dimensional Carbon Paper/Carbon Tubes/Cobalt-Sulfide Sheets as an Efficient Electrode for Overall Water Splitting. *ACS Nano* **2016**, *10*, 2342.

(22) Ai, L.; Tian, T.; Jiang, J. Ultrathin Graphene Layers Encapsulating Nickel Nanoparticles Derived Metal–Organic Frameworks for Highly Efficient Electrocatalytic Hydrogen and Oxygen Evolution Reactions. *ACS Sustain. Chem. Eng.* **2017**, *5*, 4771.

(23) Sivanantham, A.; Ganesan, P.; Shanmugam, S. Hierarchical NiCo 2 S 4 Nanowire Arrays Supported on Ni Foam: An Efficient and Durable Bifunctional Electrocatalyst for Oxygen and Hydrogen Evolution Reactions. *Adv. Funct. Mater.* **2016**, *26*, 4661.

(24) Zhang, J.; Wang, Y.; Zhang, C.; Gao, H.; Lv, L.; Han, L.; Zhang, Z. Self-Supported Porous NiSe 2 Nanowrinkles as Efficient Bifunctional Electrocatalysts for Overall Water Splitting. *ACS Sustain. Chem. Eng.* **2018**, *6*, 2231.

(25) Jiang, N.; You, B.; Sheng, M.; Sun, Y. Electrodeposited Cobalt-Phosphorous-Derived Films as Competent Bifunctional Catalysts for Overall Water Splitting. *Angew. Chemie Int. Ed.* **2015**, *54*, 6251.

(26) Wang, H.; Lee, H.-W.; Deng, Y.; Lu, Z.; Hsu, P.-C.; Liu, Y.; Lin, D.; Cui, Y. Bifunctional Non-Noble Metal Oxide Nanoparticle Electrocatalysts through Lithium-Induced Conversion for Overall Water Splitting. *Nat. Commun.* **2015**, *6*, 7261.

(27) Anantharaj, S.; Venkatesh, M.; Salunke, A. S.; Simha, T. V. S. V.; Prabu, V.; Kundu, S. High-Performance Oxygen Evolution Anode from Stainless Steel via Controlled Surface Oxidation and Cr Removal. *ACS Sustain. Chem. Eng.* **2017**, *5*, 10072.

(28) Liu, Y.; Zhang, Y.; Ma, G.; Wang, Z.; Liu, K.; Liu, H. Ethylene Glycol Reduced Graphene Oxide/polypyrrole Composite for Supercapacitor. *Electrochim. Acta* **2013**, *88*, 519.

(29) Biswas, S.; Drzal, L. T. Multilayered Nanoarchitecture of Graphene Nanosheets and Polypyrrole Nanowires for High Performance Supercapacitor Electrodes. *Chem. Mater.* **2010**, *22*, 5667.

(30) Han, Y.; Hao, L.; Zhang, X. Preparation and Electrochemical Performances of Graphite Oxide/polypyrrole Composites. *Synth. Met.* **2010**, *160*, 2336.

(31) Guan, Q.; Cheng, J.; Wang, B.; Ni, W.; Gu, G.; Li, X.; Huang, L.; Yang, G.; Nie, F. Needle-like Co 3 O 4 Anchored on the Graphene with Enhanced Electrochemical Performance for Aqueous Supercapacitors. *ACS Appl. Mater. Interfaces* **2014**, *6*, 7626.

(32) Qu, L.; Zhao, Y.; Khan, A. M.; Han, C.; Hercule, K. M.; Yan, M.; Liu, X.; Chen, W.; Wang, D.; Cai, Z.; et al. Interwoven Three-Dimensional Architecture of Cobalt Oxide Nanobrush-Graphene@Ni $_X$ Co $_{2X}$ (OH) $_{6X}$ for High-Performance Supercapacitors. *Nano Lett.* **2015**, *15* (3), 2037–2044.

(33) Ateh, D. .; Navsaria, H. .; Vadgama, P. Polypyrrole-Based Conducting Polymers and Interactions with Biological Tissues. *J. R. Soc. Interface* **2006**, *3*, 741.

(34) Yang, X.; Xu, K.; Zou, R.; Hu, J. A Hybrid Electrode of Co3O4@PPy Core/Shell Nanosheet Arrays for High-Performance Supercapacitors. *Nano-Micro Lett.* **2016**, *8*, 143.

(35) Wei, H.; He, C.; Liu, J.; Gu, H.; Wang, Y.; Yan, X.; Guo, J.; Ding, D.; Shen, N. Z.; Wang, X.; et al. Electropolymerized Polypyrrole Nanocomposites with Cobalt Oxide Coated on Carbon Paper for Electrochemical Energy Storage. *Polymer (Guildf).* **2015**, *67*, 192.

(36) Suntivich, J.; May, K. J.; Gasteiger, H. A.; Goodenough, J. B.; Shao-Horn, Y. A Perovskite Oxide Optimized for Oxygen Evolution Catalysis from Molecular Orbital Principles. *Science (80-.).* **2011**, *334*, 1383.

(37) Changzhou, Y.; Jiaoyang, L.; Linrui, H.; Xiaogang, Z.; Laifa, S.; (David), L. X. W. Ultrathin Mesoporous NiCo2O4 Nanosheets Supported on Ni Foam as Advanced Electrodes for Supercapacitors. *Adv. Funct. Mater.* **2012**, *22* (21), 4592–4597.

(38) Cheng, H.; Su, Y.-Z.; Kuang, P.-Y.; Chen, G.-F.; Liu, Z.-Q. Hierarchical NiCo2O4 Nanosheet-Decorated Carbon Nanotubes towards Highly Efficient Electrocatalyst for Water Oxidation. *J. Mater. Chem. A* **2015**, *3* (38), 19314–19321.

(39) Sing, K. S. W. Reporting Physisorption Data for Gas/solid Systems with Special Reference to the Determination of Surface Area and Porosity (Recommendations 1984). *Pure Appl. Chem.* **1985**, *57*, 603.

(40) Hu, J.; Qian, F.; Song, G.; Li, W.; Wang, L. Ultrafine MnO2 Nanowire Arrays Grown on Carbon Fibers for High-Performance Supercapacitors. *Nanoscale Res. Lett.* **2016**, *11*, 469.

(41) Bhoyate, S.; Ranaweera, C. K.; Zhang, C.; Morey, T.; Hyatt, M.; Kahol, P. K.; Ghimire, M.; Mishra, S. R.; Gupta, R. K. Eco-Friendly and High Performance Supercapacitors for Elevated Temperature Applications Using Recycled Tea Leaves. *Glob. Challenges* **2017**, *1*, 1700063.

(42) Veeramani, V.; Madhu, R.; Chen, S.-M.; Sivakumar, M. Flower-Like Nickel–Cobalt Oxide Decorated Dopamine-Derived Carbon Nanocomposite for High Performance Supercapacitor Applications. *ACS Sustain. Chem. Eng.* **2016**, *4*, 5013.

(43) Guan, Q.; Cheng, J.; Wang, B.; Ni, W.; Gu, G.; Li, X.; Huang, L.; Yang, G.; Nie, F. Needle-like Co 3 O 4 Anchored on the Graphene with Enhanced Electrochemical Performance for Aqueous Supercapacitors. *ACS Appl. Mater. Interfaces* **2014**, *6*, 7626.

(44) Zhang, C.; Wang, Z.; Bhoyate, S.; Morey, T.; Neria, B.; Vasiraju, V.; Gupta, G.; Palchoudhury, S.; Kahol, P.; Mishra, S.; et al. MoS2 Decorated Carbon Nanofibers as Efficient and Durable Electrocatalyst for Hydrogen Evolution Reaction. *C* **2017**, *3*, 33.